https://doi.org/10.1016/j.compstruct.2020.112865

DSC regularized Dirac-delta method for dynamic analysis of FG graphene platelet-reinforced porous beams on elastic foundation under a moving load

L.H. Zhang[a], **S.K. Lai**[a,b,*], **C. Wang**[a], and **J. Yang**[c]

[a] *Department of Civil and Environmental Engineering, The Hong Kong Polytechnic University, Hung Hom, Kowloon, Hong Kong, P.R. China*

[b] *Hong Kong Branch of National Rail Transit Electrification and Automation Engineering Technology Research Center, The Hong Kong Polytechnic University, Kowloon, Hong Kong, P.R. China*

[c] *School of Engineering, RMIT University, PO Box 71, Bundoora, VIC 3083, Australia*

Abstract

This work presents a novel computational approach, the DSC regularized Dirac-delta method, for the vibration analysis of functionally graded graphene-platelet reinforced (FG-GPLR) porous beams resting on a Winkler–Pasternak elastic foundation under a moving load. Based on the Timoshenko beam theory, the energy functional of the beam model is represented by a newly constructed basis function and is minimized under the variational principle. To account for the properties of composite materials, the Halpin–Tsai model is used to predict the elastic modulus of graphene-reinforced composites. A coupling of the DSC regularized Dirac-delta method and the Newmark–β integration scheme is then adopted for solving the dynamic problem. The DSC-based approach exhibits controllable accuracy for approximations and shows excellent flexibility in handling time-dependent moving load problems, because the equally spaced grid system used in the DSC numerical approach can achieve a preferable representation of moving load sources. An intensive parametric study is

*Corresponding author. E-mail address: sk.lai@polyu.edu.hk

provided with a particular focus on the influence of moving loads, foundation supports and material properties (e.g., weight fraction, porosity distribution, dispersion pattern and geometry size of graphene reinforcements). First-known solutions reported in tabular and graphical forms should be useful for researchers and engineers in designing such beam problems.

Keywords: DSC regularized Dirac-delta method, Functionally graded porous beams, Graphene-platelet reinforcement, Winkler–Pasternak foundation, Moving loads.

1. Introduction

Polymer nanocomposite materials attract considerable attention from both research and industrial communities due to their remarkable mechanical properties and chemical stability in comparison with conventional materials [1]. Since being first discovered by Iijima [2], carbon nanotubes (CNTs), with their extremely high surface-to-volume ratio, have become one of the most promising carbonaceous nanofillers to develop high-performance composite structures [3-9]. Recently, graphene platelets (GPLs), which are the two-dimensional (2D) counterparts of CNTs, have emerged as a low-cost alternative with an extremely high specific surface area [10]. Many theoretical and experimental studies indicate that a low concentration of graphene added into a pristine polymer matrix can dramatically improve its mechanical, thermal, and electrical properties as compared with the equivalent effects of CNTs [11-14]. The newly developed GPLs have shown great potential as candidates for advanced structural enhancement. This "wonder material" is more than 100 times stronger than steel but several times lighter. The strength of graphene can be exploited in composites and coatings for many reinforcement applications. In addition to mechanical strength, graphene is known as an excellent heat conductor [15]. Graphene-based materials are now commercially available and a key component of many engineering applications. For example, the production and application of porous structures, especially metal foam with low density, lightweight, good stiffness, and excellent energy absorption, have become feasible [16, 17].

Meanwhile, many efforts have been devoted to studying functionally graded material (FGM) structures [18, 19], which are characterized by a continuous spatial gradient in both material composition and properties. FGMs can improve mechanical and thermal properties, by providing several unique features that cannot be achieved by using conventional homogeneous composites, such as the alleviation of interfacial cracking or debonding due to stress concentration. The multi-functional design of

FGMs enables them to adapt to various performance conditions, and the selection of appropriate FGMs spurs the development of advanced lightweight structures [20]. To better understand the performance of FGM in practical engineering applications, Duc and his co-workers strived to investigate the buckling behavior and dynamic characteristics of FGM structures. For instance, Duc [21] provided a comprehensive study on the nonlinear static and dynamic stability of FG plates and shells. By using the third-order shear deformation theory, the nonlinear dynamic responses of FG circular cylindrical shells on an elastic foundation were studied [22, 23]. They also conducted a nonlinear and post-buckling analysis of imperfect piezoelectric FGM circular shells in the thermal environment via an analytical approach [24]. In another work, Minh and Duc [25] evaluated the stability of cracked FGM plates based on a new third-order shear deformation plate theory to discuss the influence of plate thickness ratios, crack angles and volume fractions. Besides, Vinyas and Kattimani [26, 27] further presented the static analysis of stepped FGM magneto-electro-elastic structures under various thermal loads by a finite element formulation.

Reinforced by nanofillers, the mechanical behavior of FGM structures can be further strengthened through a gradient in the volume fraction, size, shape, or orientation of the nanofillers dispersed in the matrix. Since first being isolated by Novoselov et al. [28] in 2004, graphene has sparked huge innovation in research and engineering communities. The first application of the FG concept was used to reduce the necessary concentration of CNTs and GPLs in polymer nanocomposites [29, 30]. Later, the FG concept spurred the development of a novel class of multi-layer FG carbon nanotubes reinforced (FG-CNTR) and graphene-platelet reinforced (FG-GPLR) composite structures. Inspired by this idea, numerous researchers have explored the buckling, bending and vibration analysis of such composites [6, 30-35]. In engineering applications, graphene has been widely used as a reinforcing nanofiller for polymer-based composites, its performance is highly dependent on the dispersity and distribution

of nanofillers. A comprehensive review of this emerging area, covering the mechanical properties, fabrication procedures, and current challenges for FG-GPLR composites, has been carried out recently [20].

In the last few decades, many research studies on moving load problems that have been well-documented in the literature mainly focused on conventional homogeneous and inhomogeneous composite structures, e.g., steel, concrete and FGM. For example, Yang et al. [36] made use of a simple beam model to evaluate the condition of resonance excited by a high-speed moving load. Law and Zhu [37] applied a four-degree-of-freedom coupling model to investigate the dynamic behavior of damaged reinforced concrete structures. Yang et al. [38] investigated the crack effect of inhomogeneous beams under free and forced vibration motions. Kim [39] presented the dynamic response of an axially loaded beam excited by a moving load. In addition, Malekzadeh and Monajjemzadeh [40] analyzed the dynamic response of FGM beams in the thermal environment. He and Zhu [41] investigated the moving load-induced response of damaged beams. Svedholm et al. [42] devised an analytical approach for evaluating the dynamic response of non-proportionally damped beams under a moving load. More recently, Zhang et al. [43] further dealt with the moving load problem of FGM beams with rotational elastic edge constraints.

The dynamic interaction of beam-type structures resting on various elastic foundations under concentrated moving loads is of fundamental importance to the engineering community. Such beam systems can be found in a variety of engineering applications, e.g., bridges, roadways and rails [44-47]. In structural dynamics, this specific topic refers to any structures subjected to loads that move in space and excite the structures into vibration. Investigation such time-dependent problems can optimize the structural design and ensure the stability and reliability of structures in real-engineering conditions. From a theoretical point of view, both structures and moving

loads can be regarded as two coupled elastic systems that interact with each other through the contact force [44].

Furthermore, the impact of supporting foundations on the dynamic behavior of beams subjected to moving loads is another crucial topic. The foundation of structures can be divided into shallow and deep foundations that are used to transfer loadings from heavy structures to underneath layers, in which the shallow one can be modeled by beam and plate structures [48]. Both Winkler and Pasternak elastic models are commonly used to represent an idealization of the soil medium by a number of mutually independent spring elements [48, 49]. The first model assumes that the contact pressure at any point is proportional to the settlement of the soil medium at that point and it is not dependent on the deflection at other locations. The second type is a two-parameter model that can be used to account for the shear interaction between the spring elements. This is accomplished by connecting the ends of the springs to its connected structures with incompressible vertical elements that can deform in transverse shear only [50].

Using the Winkler and Pasternak elastic foundation models, Çalım [51] considered the influence of time-dependent loads on the vibration behavior of shear deformable beams. Yan et al. [52] characterized the dynamic properties of edge-cracked shear deformable FGM beams under a moving load. Şimşek et al. [53] conducted a linear dynamic analysis on the flexural vibration of an axially FGM beam due to a moving harmonic load. Lee et al. [54] determined the natural frequencies for the bending and twisting motions of beams. Deng et al. [55] further carried out the vibration and buckling studies on a double-FGM beam using the Wittrick–William algorithm. Recently, Qaderi et al. [56] provided the free vibration analysis of graphene-reinforced composite beams resting on a viscoelastic foundation. Moreover, Froio et al. [57] also derived the steady-state solutions for a uniform infinite Euler–Bernoulli beam under a constant moving force.

Investigation of moving load problems always involves the use of a unit impulse function, i.e., the Dirac-delta function. From a computational point of view, the weak-form based approaches e.g., the Ritz method and the finite element method can easily handle such problems by directly integrating the governing differential equations, while there still exist some difficulties using the strong-form based numerical algorithms, such as the differential quadrature method (DQM) and the finite difference method. As reported by Eftekhari [58], the computational solutions of the collocation method for the Dirac-type function become oscillatory around singularities because of the Gibbs phenomenon. Hence, such a singular function should be regularized to achieve a smoother representation and computational stability according to the work of Gheorghiu [59]. A regularization of the Gaussian smooth function is thus used to replace the time-dependent singular function.

Indeed, various forms of the regularized Dirac-delta function have been proposed in the DSC context [60]. Based on the theory of distribution and wavelet analysis, the DSC approach possesses good accuracy and stability and has been well applied to handle various engineering problems [61-63]. To go beyond the limitation of the conventional DSC approach, the authors recently proposed a DSC regularized Dirac-delta method for moving load problems [43]. The results indicated that the evenly distributed grid system of the DSC scheme provides a simple representation of moving load sources as compared to the DQM. Besides, the DSC sparse matrix enables trade-offs between computational effort and accuracy. With the encouragement of this study, for the first time, we investigate the coupling interaction among moving loads, graphene-reinforced structures and supporting foundations as a whole by means of this new approach in the present work.

Despite the aforementioned extensive research on various FG-GPLR composite structures [20], to the authors' best knowledge, no solutions are hitherto available in

the literature for the dynamic analysis of shear deformable FG-GPLR beams resting on a Winkler–Pasternak elastic foundation under a moving load. Prompted by the lack of research work in this area, this work aims to fill this apparent gap by providing accurate results for such a problem. Results of the present study will facilitate the design of advanced lightweight composite structures in civil and mechanical engineering, e.g., the importance of nanofillers' dispersity and the application of foundation structures. Making use of the Timoshenko beam theory [64] and the Halpin–Tsai model [65], the governing equations of motion that account for the effects of transverse shear, rotary inertia and nanocomposite behavior are formulated.

In this work, a two-level discretization (i.e., spatial and temporal) is involved. The first procedure is the implementation of the DSC regularized Dirac-delta approach to approximate the governing equations, and the second one is to apply the Newmark–β integration scheme [66] to discretize the time derivatives. First-known vibration solutions and dynamic magnification factors for this beam problem resting on the elastic foundations are obtained and presented in tabular and graphical forms. The influence of the foundation stiffness parameters, porosity distributions, dispersion patterns and moving excitation forces is also studied. The present results will serve as benchmark checks for researchers to verify their numerical methods and are also important for engineers to design FG-GPLR porous beams supported by elastic foundations under the effect of moving loads in engineering practice.

2. Material Properties of FG-GPLR Porous Beams

Consider an FG-GPLR porous beam supported by a Winkler–Pasternak elastic foundation with length L, width b, and thickness h in Fig.1. A Cartesian coordinate system (x, z) is established where the x-axis locates on the mid-plane and the z-axis is along the thickness direction. The material properties of the FG-GPLR porous beam are supposed to change due to the variation of size and the density of internal pores

during the manufacturing process. The FG porosities that vary along the beam thickness can be classified into four different types, i.e., one asymmetric distribution, two symmetric distributions, and one uniform distribution as shown in Fig. 2. To further strengthen the mechanical properties, GPLs are utilized as nanofillers to reinforce the metal matrix of the FG-GPLR beam, having three dispersion patterns as illustrated in Fig. 3. The FG-GPLR beam is subjected to a concentrated moving load f, which moves along the axial direction with a constant velocity v_p. This moving force enters the beam at $t = 0$ and leaves at $t = v_p/L$. The elastic foundation considered in this work is a Winkler–Pasternak type, having a shear layer and a spring layer.

It is assumed that the porosity of the beam would change in the thickness direction and the effective properties may vary from the bottom surface ($z = -h/2$) to the top surface ($z = h/2$). The Young's modulus $E(z)$, shear modulus $G(z)$ and mass density $\rho(z)$ are expressed as [67, 68]

$$\begin{aligned} E(z) &= E_{max}[1 - e_0\alpha(z)] \\ G(z) &= G_{max}[1 - e_0\alpha(z)] \\ \rho(z) &= \rho_{max}[1 - e_d\alpha(z)] \end{aligned} \tag{1}$$

where E_{max}, G_{max} and ρ_{max} are the Young's modulus, shear modulus, and mass density of the FG-GPLR beam without any internal pores, respectively. e_0 $(= 1 - E_{min}/E_{max})$ and e_d $(= 1 - \rho_{min}/\rho_{max})$ are the porosity coefficient and mass density coefficient, respectively. E_{min}, G_{min} and ρ_{min} are the minimum corresponding values of material properties. $\alpha(z)$ is a porosity distribution type given by [68]

$$\alpha(z) = \begin{cases} \cos(\pi z/h) & Porosity\ distribution\ type\ 1 \\ cos(\pi z/2h + \pi/4) & Porosity\ distribution\ type\ 2 \\ cos(|\pi z/h| - \pi/2) & Porosity\ distribution\ type\ 3 \\ \alpha^* & Uniform\ distribution \end{cases} \tag{2}$$

According to the closed-cell Gaussian Random Field (GRF) scheme for cellular solids [69], the relationship between the Young's modulus and the mass density can be established using the following equation

$$\frac{E(z)}{E_{max}} = \left(\frac{\rho(z)/\rho_{max} + 0.121}{1.121}\right)^{2.3} \qquad \left(0.15 < \frac{\rho(z)}{\rho_{max}} < 1\right) \tag{3}$$

Then, the mass density coefficient e_d is expressed by Eqs. (1) and (3) as

$$e_d = \frac{1.121\left(1 - \sqrt[2.3]{1 - e_0\alpha(z)}\right)}{\alpha(z)} \tag{4}$$

To follow the assumption of the closed-cell metal foam, the permissible value of the maximum porosity coefficient e_0 can be calculated by substituting Eqs. (1) and (4) into the ratio range of Eq. (3). Then, we have

$$0.15 < 1 - 1.121\left(1 - \sqrt[2.3]{1 - e_0\alpha(z)}\right) < 1 \quad \rightarrow \quad 0 < e_0 < 0.9618 \tag{5}$$

The porosity coefficient e_0 should be smaller than 0.9618 for FG-GPLR closed-cell metal foam composite structures.

For a fair and meaningful comparison, various combinations between porosity distributions and GPL dispersion patterns are carried out. The total mass M of the FG-GPLR porous beam is defined by [32, 68]

$$M = \int_{-h/2}^{h/2} \rho(z)\, dz \tag{6}$$

Upon substituting Eq. (6) to Eq. (1) with Eq. (3), α^* (i.e., the uniform distribution pattern) in Eq. (2) is derived as follows

$$\alpha^* = \frac{1}{e_0}\left[1 - \left(\frac{M/\rho_{max}h + 0.121}{1.121}\right)^{2.3}\right] \tag{7}$$

The relationship of the Young's modulus and shear modulus of FG-GPLR porous beams is

$$G(z) = \frac{E(z)}{2\left(1+\nu(z)\right)} \tag{8}$$

where the Poisson's ratio $\nu(z)$ of closed-cell cellular structures can be written as [70]

$$\nu(z) = 0.342\nu_{max}\left(\frac{\rho(z)}{\rho_{max}}\right)^2 + (0.526\nu_{max} - 0.221)\frac{\rho(z)}{\rho_{max}} + 0.132\nu_{max} + 0.221 \tag{9}$$

in which ν_{max} denotes the Poisson's ratio of metal without internal pores.

Based on the Halpin–Tsai micromechanical model [65, 71], it is assumed that a non-porous FG-GPLR metal matrix is randomly oriented in fiber-reinforced composites. Therefore, the maximum Young's modulus E_{max} of the FG-GPLR beam can be calculated by [32, 68, 72, 73]

$$E_{max} = \left[\frac{3}{8}\left(\frac{1+\gamma_L^{GPL}\epsilon_L^{GPL}V_{GPL}}{1-\epsilon_L^{GPL}V_{GPL}}\right) + \frac{5}{8}\left(\frac{1+\gamma_W^{GPL}\epsilon_W^{GPL}V_{GPL}}{1-\epsilon_W^{GPL}V_{GPL}}\right)\right]E_M \tag{10}$$

in which γ_L^{GPL} and γ_W^{GPL} take the influence of the geometry and size of graphene reinforcements as

$$\gamma_L^{GPL} = 2\left(\frac{l_{GPL}}{h_{GPL}}\right), \quad \gamma_W^{GPL} = 2\left(\frac{w_{GPL}}{h_{GPL}}\right) \tag{11}$$

and l_{GPL}, w_{GPL} and h_{GPL} denote the average length, width, and thickness of GPLs in composite beams. In Eq. (10), the parameters ϵ_L^{GPL} and ϵ_W^{GPL} are defined by

$$\epsilon_L^{GPL} = \frac{(E_{GPL}/E_M)-1}{(E_{GPL}/E_M)+\gamma_L^{GPL}}, \quad \epsilon_W^{GPL} = \frac{(E_{GPL}/E_M)-1}{(E_{GPL}/E_M)+\gamma_W^{GPL}} \tag{12}$$

where E_{GPL} and E_M are the Young's modulus of GPLs and metal matrix, respectively. Then, the mass density ρ_{max} and the Poisson's ratio ν_{max} can be calculated by the following rule of mixture [32, 68, 72, 73]

$$\begin{aligned} \rho_{max} &= \rho_{GPL}V_{GPL} + \rho_M V_M \\ \nu_{max} &= \nu_{GPL}V_{GPL} + \nu_M V_M \end{aligned} \tag{13}$$

in which the subscripts indicate the material properties of GPLs and metal matrix. The relationship of two volume fractions is expressed as $V_{GPL} + V_M = 1$. As shown in Fig.

3, the arrangement of GPLs is assumed to vary along the beam thickness according to the following three dispersion patterns [32, 68, 74]

$$V_{GPL} = \begin{cases} P_{i1}[1 - cos(\pi z/h)] & Pattern\ A \\ P_{i2}[1 - cos(\pi z/2h + \pi/4)] & Pattern\ B \\ P_{i3} & Pattern\ C \end{cases} \tag{14}$$

where P_{i1}, P_{i2}, and P_{i3} are the peak values for various types of GPL patterns and can be further obtained through the same nanofiller weight fraction Γ_{GPL} [32, 68, 74]

$$\frac{\Gamma_{GPL}\rho_M \int_{-h/2}^{h/2}[1 - e_d\alpha(z)]dz}{\Gamma_{GPL}\rho_M + (1 - \Gamma_{GPL})\rho_{GPL}} = \int_{-h/2}^{h/2} V_{GPL}[1 - e_d\alpha(z)]dz \tag{15}$$

3. Theoretical Formulation of FG-GPLR Porous Beam Model

Based on the Timoshenko beam theory [75], the displacement components ($U(x,y,z)$ and $W(x,y,z)$) of an arbitrary point in the beam along the x and z directions are

$$\begin{aligned} U(x,y,z) &= u_0(x,t) - z\phi(x,t) \\ W(x,y,z) &= w_0(x,t) \end{aligned} \tag{16}$$

where $w_0(x,t)$ and $u_0(x,t)$ are the transverse and axial displacement components at the mid-plane of the beam $(z = 0)$, respectively. $\phi(x,t)$ denotes the cross-section rotation, and t is time. Based on the linear strain-displacement relations, the longitudinal strain ε_{xx} and the transverse shear strain γ_{xz} can be calculated as

$$\begin{aligned} \varepsilon_{xx} &= \frac{\partial u_0}{\partial x} - z\frac{\partial \phi}{\partial x} \\ \gamma_{xz} &= \frac{\partial w_0}{\partial x} - \phi \end{aligned} \tag{17}$$

Then, the normal stress σ_{xx} and the transverse stress τ_{xz} can be expressed using the following linear stress-strain constitutive law

$$\begin{aligned} \sigma_{xx} &= \frac{E(z)}{1 - \nu(z)^2}\varepsilon_{xx} \\ \tau_{xz} &= G(z)\gamma_{xz} \end{aligned} \tag{18}$$

The kinetic energy (T) of the present system is expressed as

$$T = \frac{b}{2}\int_0^l \int_{-h/2}^{h/2} \rho(z)\left[\left(\frac{\partial U}{\partial t}\right)^2 + \left(\frac{\partial W}{\partial t}\right)^2\right] dzdx \tag{19}$$

Substituting Eq. (16) into Eq. (19) yields

$$T = \frac{b}{2}\int_0^l \left[I_0\left(\frac{\partial u_0}{\partial t}\right)^2 - I_1\frac{\partial u_0}{\partial t}\frac{\partial \phi}{\partial t} + I_2\left(\frac{\partial \phi}{\partial t}\right)^2 + I_0\left(\frac{\partial w_0}{\partial t}\right)^2\right] dx \tag{20}$$

in which the inertia terms (I_0, I_1, I_2) are defined by

$$(I_0, I_1, I_2) = \int_{-h/2}^{h/2} \rho(z)(1, z, z^2)dz \tag{21}$$

The potential energy of the present system consists of the strain energy V_s and the other one due to the Winkler–Pasternak foundation V_w. Consider the strain energy V_s, we have

$$V_s = \frac{b}{2}\int_0^l \int_{-h/2}^{h/2} (\sigma_{xx}\varepsilon_{xx} + \tau_{xz}\gamma_{xz})\, dzdx \tag{22}$$

Making use of Eqs. (17) and (18), the strain energy V_s in terms of the mid-plane rotation and displacements is given as

$$\begin{aligned} V_s = \frac{b}{2}\int_0^l \Bigg[& A_{11}\left(\frac{\partial u_0}{\partial x}\right)^2 - 2B_{11}\frac{\partial u_0}{\partial x}\frac{\partial \phi}{\partial x} + D_{11}\left(\frac{\partial \phi}{\partial x}\right)^2 + A_{55}\left(\frac{\partial w_0}{\partial x}\right)^2 \\ & - 2A_{55}\frac{\partial w_0}{\partial x}\phi + A_{55}\phi^2\Bigg] dx \end{aligned} \tag{23}$$

where the stiffness elements A_{11}, B_{11}, D_{11}, and A_{55} are

$$\begin{aligned} (A_{11}, B_{11}, D_{11}) &= \int_{-h/2}^{h/2} \frac{E(z)}{1-\nu(z)^2}(1, z, z^2)dz \\ A_{55} &= \int_{-h/2}^{h/2} \kappa G(z)dz \end{aligned} \tag{24}$$

in which $\kappa = 5/6$ is the shear correction factor. The potential energy V_w resulted by the Winkler–Pasternak elastic foundation is given by

$$V_w = \frac{b}{2}\int_0^l \left[K_1 {w_0}^2 + K_2\left(\frac{\partial w_0}{\partial x}\right)^2\right] dx \tag{25}$$

where K_1 and K_2 are the modulus of the Winkler foundation and the shear layer foundation stiffness of the Pasternak model, respectively.

Eventually, the work done by an external moving force is Q presented as

$$Q = b\int_0^l f\delta(x - v_p t)w_0 dx \tag{26}$$

where $\delta(\cdot)$ is the Dirac-delta function, and v_p represents the velocity of a moving load.

According to Hamilton's principle, the governing equations of the FG-GPLR porous beam resting on the Winkler–Pasternak elastic foundation are derived by

$$\Pi = \delta\int_{t_1}^{t_2}[T - (V_s + V_w) + Q]dt \tag{27}$$

in which δ indicates the virtual variation of the energy of the system. The expressions of δT, δV_s, δV_w and δQ are presented in Appendix A. Substituting Eqs. (A1)–(A4) (i.e., δT, δV_s, δV_w and δQ) into Eq. (27) and rearranging the coefficients of δu_0, $\delta\phi$, and δw_0, we derive the dynamic equilibrium equations of the FG-GPLR porous beam resting on the Winkler–Pasternak elastic foundation under a moving load as follows

$$\delta u_0: \quad A_{11}\frac{\partial^2 u_0}{\partial x^2} - B_{11}\frac{\partial^2 \phi}{\partial x^2} = I_0\frac{\partial^2 u_0}{\partial t^2} - I_1\frac{\partial^2 \phi}{\partial t^2} \tag{28}$$

$$\delta\phi: \quad -B_{11}\frac{\partial^2 u_0}{\partial x^2} + D_{11}\frac{\partial^2 \phi}{\partial x^2} + A_{55}\left(\frac{\partial w_0}{\partial x} - \phi\right) = -I_1\frac{\partial^2 u_0}{\partial t^2} + I_2\frac{\partial^2 \phi}{\partial t^2} \tag{29}$$

$$\delta w_0: \quad A_{55}\left(\frac{\partial^2 w_0}{\partial x^2} - \frac{\partial \phi}{\partial x}\right) - K_1 w_0 + K_2\frac{\partial^2 w_0}{\partial x^2} = I_0\frac{\partial^2 w_0}{\partial t^2} - f\delta(x - v_p t) \tag{30}$$

By introducing the following dimensionless parameters

$$\begin{gathered}\xi = \frac{x}{L}, \eta = \frac{L}{h}, \{U_0, W_0\} = \frac{\{u_0, w_0\}}{h}, \Phi = \phi, \tau = t\sqrt{\frac{A^*}{I^* L^2}}, V = v_p\sqrt{\frac{I^*}{A^*}}, \\ \{a_{11}, b_{11}, d_{11}, a_{55}\} = \left\{\frac{A_{11}}{A^*}, \frac{B_{11}}{A^* h}, \frac{D_{11}}{A^* h^2}, \frac{A_{55}}{A^*}\right\}, \{k_1, k_2\} = \left\{\frac{K_1 L^2}{A^*}, \frac{K_2}{A^*}\right\},\end{gathered} \tag{31}$$

$$\{i_0, i_1, i_2\} = \left\{\frac{I_0}{I^*}, \frac{I_1}{I^* h}, \frac{I_2}{I^* h^2}\right\}, \lambda = \omega L \sqrt{\frac{I^*}{A^*}}, F = \frac{fL}{A^* h}$$

in which A^* and I^* represent the values of A_{11} and I_0, they are the corresponding values of a pure metal beam without any pores and nanofillers. F and λ denote the non-dimensional moving force and the non-dimensional natural frequency parameter, respectively. Hence, the dimensionless equations of motion can be rewritten as

$$a_{11}\frac{\partial^2 U_0}{\partial \xi^2} - b_{11}\frac{\partial^2 \Phi}{\partial \xi^2} = i_0\frac{\partial^2 U_0}{\partial \tau^2} - i_1\frac{\partial^2 \Phi}{\partial \tau^2} \tag{32}$$

$$-b_{11}\frac{\partial^2 U_0}{\partial \xi^2} + d_{11}\frac{\partial^2 \Phi}{\partial \xi^2} + a_{55}\left(\eta\frac{\partial W_0}{\partial \xi} - \eta^2 \Phi\right) = -i_1\frac{\partial^2 U_0}{\partial \tau^2} + i_2\frac{\partial^2 \Phi}{\partial \tau^2} \tag{33}$$

$$a_{55}\left(\frac{\partial^2 W_0}{\partial \xi^2} - \eta\frac{\partial \Phi}{\partial \xi}\right) - k_1 W_0 + k_2\frac{\partial^2 W_0}{\partial \xi^2} = i_0\frac{\partial^2 W_0}{\partial \tau^2} - F\delta(\xi - V\tau) \tag{34}$$

4. DSC Regularized Dirac-delta Method

Based on the theory of distributions and the theory of wavelets, a singular convolution is defined by [60]

$$F(t) = (T * \eta)(t) = \int_{-\infty}^{\infty} T(t - x)\eta(x)\, dx \tag{35}$$

where $\eta(t)$ denotes an element of the space of test functions, T is assumed to be a distribution with various forms, and $T(t - x)$ is a singular kernel. Depending on different application scenarios in science and engineering problems, various types of singular kernels of T can be used. The delta type, especially the high-order kernels ($n > 1$), is essential for handling partial differential equations. In order to overcome the difficulty of directly using singular expressions, a sequence of approximation can be constructed by [60]

$$\lim_{\varepsilon \to \varepsilon_0} T_\varepsilon(x) \to T(x) \tag{36}$$

where ε_0 denotes a generalized limit. Every single element in the sequence, $T_\varepsilon(x)$, is a delta sequence kernel when applying a singular kernel of the delta type ($\delta^{(n)}(x)$) to $T(x)$. Consider a sufficiently smooth approximation, DSC is defined as [60]

$$F_\varepsilon(t) = \sum_k T_\varepsilon\,(t - x_k) f(x_k) \tag{37}$$

where $F_\alpha(t)$ approximates $F(t)$ corresponding to a set of discrete points $\{x_k\}$. The Dirac-delta function is a generalized function that can be integrable inside an interval but itself does not need to have a value. To properly apply the delta type of singular kernels, we introduce a Schwartz class function [60], i.e., the Gaussian regularizer R_ε, as follows

$$R_\varepsilon(x) = \exp\left(-\frac{x^2}{2\varepsilon^2}\right) \tag{38}$$

For the limiting cases, we have

$$\lim_{\varepsilon\to\infty} R_\varepsilon(x) = 1 \tag{39}$$

and

$$R_\varepsilon(0) = 1 \tag{40}$$

Once we apply this regularizer to a Dirac-delta type kernel function, an immediate benefit obtained is that its Fourier transform is infinitely differentiable. For example, the widely used regularized Shannon's sequence kernel is written as [60]

$$\delta_\varepsilon\ (x) = \frac{\sin(\pi x)}{\pi x}\exp\left(-\frac{x^2}{2\varepsilon^2}\right) \tag{41}$$

As aforementioned, a moving point load can be represented by the Dirac-delta function $\delta(\cdot)$. Applying a strong-form based method is difficult for this problem, because the special feature of this time-dependent singular function depends on [76]

$$\int_{-\infty}^{+\infty} \delta\big(x - x_p\big)\, dx = 1 \tag{42}$$

and

$$\int_{-\infty}^{+\infty} f(x)\delta\big(x - x_p\big)\, dx = f(x_p) \tag{43}$$

The Gauss' delta sequence function that can satisfy the above conditions shows a sufficiently smooth approximation, as given by [60]

$$\delta_\varepsilon(x) = \frac{1}{\sqrt{2\pi}\varepsilon}\exp\left(-\frac{x^2}{2\varepsilon^2}\right) \tag{44}$$

To obviate the limitation of the strong-form based method in handling such a time-dependent problem, the Dirac-delta function is replaced by a discretized form of the Gauss' delta function in Eq. (44) as follows

$$\delta_\varepsilon(x-x_0) \approx \frac{1}{\sqrt{2\pi}\varepsilon}\exp\left[-\frac{(x-x_0)^2}{2\varepsilon^2}\right] \quad \text{for } \varepsilon \to 0 \tag{45}$$

where ε is a parameter to control the smoothness and accuracy of representations. The selection of a very small value of ε will increase the number of grid points for computation. Therefore, a proper value of ε to balance numerical accuracy and computational cost is required.

Based on Eq. (45), a moving load source is thus approximated by

$$F\delta\left(\xi-\xi_p(t)\right) = \frac{fL}{A^* h\sqrt{2\pi}\varepsilon}\exp\left[-\frac{\left(\xi-\xi_p(t)\right)^2}{2\varepsilon^2}\right] \tag{46}$$

in which $\xi_p(t) = V\tau\left(i.e., v_p/L\right)$ is a dimensionless coordinate of the traveling force. By neglecting the axial inertial term with small influence and substituting Eq. (46) into Eq. (34), the governing equations can be further reduced to the following form

$$\begin{aligned} a_{55}\left(\frac{\partial^2 W_0}{\partial\xi^2}-\eta\frac{\partial\Phi}{\partial\xi}\right) - k_1 W_0 + k_2\frac{\partial^2 W_0}{\partial\xi^2} \\ = i_0\frac{\partial^2 W_0}{\partial\tau^2} - \frac{F}{\sqrt{2\pi}\varepsilon}\exp\left[-\frac{\left(\xi-\xi_p(t)\right)^2}{2\varepsilon^2}\right] \end{aligned} \tag{47}$$

$$\left(d_{11}-\frac{{b_{11}}^2}{a_{11}}\right)\frac{\partial^2\Phi}{\partial\xi^2} + a_{55}\left(\eta\frac{\partial W_0}{\partial\xi}-\eta^2\Phi\right) = \left(i_2-\frac{b_{11}i_1}{a_{11}}\right)\frac{\partial^2\Phi}{\partial\tau^2} \tag{48}$$

According to the DSC algorithm, the *r*-th order derivatives of an arbitrary function $f(x)$ with respect to a set of points $(x_1, x_2, x_3, \ldots, x_N)$ can be approximated by [60, 77, 78]

$$f^{(r)}(x) \approx \sum_{m=-M}^{M} C_m^r f(x_m) \tag{49}$$

where M is called the half computational bandwidth; $f(x_m)$ is regarded as a trial function; C_m^r denotes weighting coefficients for r-th order derivative approximation which is calculated through the Dirac-delta function. The regularized Shannon's delta kernel function in Eq. (41) can be discretized as [60]

$$\delta_{\sigma,\Delta}(x - x_m) = \frac{\sin\left[\left(\frac{\pi}{\Delta}\right)(x - x_m)\right]}{\left(\frac{\pi}{\Delta}\right)(x - x_m)} \exp\left[-\frac{(x - x_m)^2}{2\sigma^2}\right] \tag{50}$$

where $\Delta = 1/(N-1)$ is the grid spacing, x_m is the grid point coordinate and $m = -M, -M+1, \ldots, 0, M-1, M$; σ determines the effective computational bandwidth. By employing a dimensionless weighted linear combination of the function values at uniformly distributed points $(2M+1)$ as

$$0 = \xi_0 < \xi_1 < \cdots \xi_m < \cdots < \xi_{N-1} = 1, \quad k = 0,1 \ldots, N-1 \tag{51}$$

It is worth noting that some commonly used numerical methods, such as the Galerkin approach and finite difference method, can be derived from a single starting point by the implementation of the DSC algorithm to offer a unified representation [60]. In addition, the DSC approach has been authenticated as an ingenious mean for the stability and dynamic analysis of various structures due to its high-level of accuracy and excellent flexibility in handling complex geometries and boundary conditions [79, 80]. A small matrix-band in the approximation of partial derivatives resulted from Eq. (49) enhances computational efficiency especially for a large-scale structural analysis [43]. This newly proposed DSC regularized Dirac delta approach not only can effectively address the difficulties of strong-form methods in dealing with moving load problems, but also provide a preferable representation of moving load sources with the same order of discretized errors regardless of the location of a moving load by using the equally spaced grid system as shown in Eq. (55). A comparison study with the DQM has been carried out in the previous work [43].

An $N \times N$ differentiation matrix $\mathbf{D}_q^r (q = \xi \; or \; \gamma, \; r = 1,2, \ldots)$ is defined as follows

$$\left[\mathbf{D}_q^r\right] = \delta_{\alpha,\Delta}^{(r)}(q_i - q_m) = \left[\left(\frac{d}{dx}\right)^r \delta_{\alpha,\Delta}(q - q_m)\right]_{q=q_i} = C_m^r \tag{52}$$

It is noted that there remain M fictitious points (also known as ghost points) out of the physical domain when applying the DSC method as indicated in Eq. (49), as shown in Fig. 4. The symmetric and anti-symmetric methods are employed for the treatment of simply supported and clamped edges [60, 79, 80], respectively. The basic idea is to establish the relationship between the inner and outer points. For example, the lateral deflection of a beam at the left side is presented as [60]

$$W(\xi_{-m}) - W(\xi_0) = a_m^W[W(\xi_m) - W(\xi_0)] \tag{53}$$

which is easy to be arranged as

$$W(\xi_{-m}) = a_m^W W(\xi_m) + (1 - a_m^W)W(\xi_0) \tag{54}$$

where a_m^W (or a_m^Φ) is an assumptive coefficient for different displacements. The first- and second-order derivatives of W are given by

$$\begin{aligned} W'(\xi) &= \sum_{m=-M}^{M} C_m^1 W(\xi_m) \\ &= \left[C_0^1 - \sum_{m=1}^{M}(1 - a_m^W)C_m^1\right]W(\xi_0) + \sum_{m=1}^{M}(1 - a_m^W)C_m^1 W(\xi_m) \end{aligned} \tag{55}$$

$$\begin{aligned} W''(\xi) &= \sum_{m=-M}^{M} C_m^2 W(\xi_m) \\ &= \left[C_0^2 + \sum_{m=1}^{M}(1 - a_m^W)C_m^2\right]W(\xi_0) + \sum_{m=1}^{M}(1 + a_m^W)C_m^2 W(\xi_m) \end{aligned} \tag{56}$$

Consider simply supported boundaries (S) (i.e., $W(\xi) = \Phi(\xi) = 0$) and clamped supports (C) (i.e., $W(\xi) = \partial\Phi(\xi)/\partial\xi = 0$), we have

S: $W(\xi_{-m}) = -W(\xi_m), \quad \Phi(\xi_{-m}) = \Phi(\xi_m), \ (a_m^W = -1 \ and \ a_m^\Phi = 1)$ (57)

C: $W(\xi_{-m}) = W(\xi_m), \quad \Phi(\xi_{-m}) = -\Phi(\xi_m), \ (a_m^W = 1 \ and \ a_m^\Phi = -1)$ (58)

Following the above procedures, the DSC regularized Dirac-delta method is formulated, in which two Dirac-delta kernels are incorporated to approximate the

moving load source and the governing equations. Having eliminated the ghost points in the DSC scheme, the governing equilibrium Eqs. (47) and (48) can be further presented in a matrix notation as follows

$$\begin{bmatrix}\mathbf{K}_{aa} & \mathbf{K}_{ab}\\ \mathbf{K}_{ba} & \mathbf{K}_{bb}\end{bmatrix}\begin{Bmatrix}\boldsymbol{W}_{\mathbf{0}}(t)\\ \boldsymbol{\Phi}(t)\end{Bmatrix}+\begin{bmatrix}\mathbf{M}_{aa} & \mathbf{M}_{ab}\\ \mathbf{M}_{ba} & \mathbf{M}_{bb}\end{bmatrix}\begin{Bmatrix}\ddot{\boldsymbol{W}}_{\mathbf{0}}(t)\\ \ddot{\boldsymbol{\Phi}}(t)\end{Bmatrix}=\begin{Bmatrix}\boldsymbol{F}(t)\\ \mathbf{0}\end{Bmatrix} \tag{59}$$

where the elements of these matrices and vectors are presented in Appendix B. This second-order differential equation containing the time-dependent coefficient matrices can be solved by time integration schemes. This study utilizes the Newmark–β integration scheme [81] with good stability for the concerned problem.

For free vibration analysis, the external moving force is assumed to be zero and the sinusoidal motion is applied as

$$W_0(\xi,t)=\bar{W}(\xi)\cos(\omega t)\,,\quad \Phi(\xi,t)=\bar{\Phi}(\xi)\cos(\omega t) \tag{60}$$

where ω is the circular frequency of vibration. Then, substituting Eq. (60) into Eqs. (47) and (48) results in

$$a_{55}\left(\frac{\partial^2\bar{W}}{\partial\xi^2}-\eta\frac{\partial\bar{\Phi}}{\partial\xi}\right)-k_1\bar{W}+k_2\frac{\partial^2\bar{W}}{\partial\xi^2}=-i_0\omega^2\bar{W} \tag{61}$$

$$\left(d_{11}-\frac{{b_{11}}^2}{a_{11}}\right)\frac{\partial^2\bar{\Phi}}{\partial\xi^2}+a_{55}\left(\eta\frac{\partial\bar{W}}{\partial\xi}-\eta^2\bar{\Phi}\right)=\left(\frac{b_{11}i_1}{a_{11}}-i_2\right)\omega^2\bar{\Phi} \tag{62}$$

In terms of a matrix form, Eqs. (61) and (62) can be expressed as follows

$$\begin{bmatrix}\widetilde{\mathbf{K}}_{aa} & \widetilde{\mathbf{K}}_{ab}\\ \widetilde{\mathbf{K}}_{ba} & \widetilde{\mathbf{K}}_{bb}\end{bmatrix}\begin{Bmatrix}\overline{\boldsymbol{W}}(\xi)\\ \bar{\boldsymbol{\Phi}}(\xi)\end{Bmatrix}=\lambda^2\begin{Bmatrix}\overline{\boldsymbol{W}}(\xi)\\ \bar{\boldsymbol{\Phi}}(\xi)\end{Bmatrix} \tag{63}$$

where λ is a non-dimensional natural frequency and the matrix elements are provided in Appendix B. Finally, Eq. (63) can be solved by a standard eigenvalue solver.

5. Results and Discussion

To investigate the dynamic characterization of FG-GPLR porous beams resting on the Winkler–Pasternak foundation under a moving load, illustrative numerical examples by the DSC method are provided herein. Effects of various parameters on the

natural frequencies and mid-span deflection of FG-GPLR porous beams with different boundary conditions are also discussed.

As shown in Figs. 2 and 3, four types of porosity distributions (1, 2, 3 and 4) and three kinds of GPL patterns (A, B and C) are considered in this work. It is worth noting that the porosity distribution types 1 and 3 and the pattern A are nonlinearly symmetric, while the porosity distribution type 2 and the pattern B are both nonlinearly asymmetric across the thickness direction. The porous and GPL nanofillers are evenly distributed in the porosity distribution type 4 and the pattern C, respectively. In this work, copper, having the material properties $E_c = 130$ GPa, $\rho_c = 8960$ kg/m^3, and $\nu_c = 0.34$, is one of the commonly used metals to serve as a matrix material. The material properties of GPLs [32, 71] are $E_{GPL} = 1.01$ TPa, $\rho_{GPL} = 1062.5$ kg/m^3 and $\nu_{GPL} = 0.186$, and the geometry dimensions are $w_{GPL} = 1.5$ μm, $l_{GPL} = 2.5$ μm and $h_{GPL} = 1.5$ nm.

5.1 Convergence and validation of present study (simple FG beams)

The free vibration analysis of FG-GPLR porous beams supported by the Winkler–Pasternak foundation is carried out in this study. As there are no existing solutions available in the open literature for the problem being considered, the free vibration analysis of FG beams with or without an elastic foundation is studied to examine the accuracy and validity of the present analysis.

Based on the following power-law functions, the material properties of an FG beam, including elasticity modulus $\bar{E}(z)$, shear modulus $\bar{G}(z)$ and mass density $\bar{\rho}(z)$, are calculated as follows [82-85]

$$\begin{aligned} \bar{E}(z) &= (E_t - E_b)\left(\frac{z}{h} + \frac{1}{2}\right)^k + E_b \\ \bar{G}(z) &= (G_t - G_b)\left(\frac{z}{h} + \frac{1}{2}\right)^k + G_b \end{aligned} \tag{64}$$

$$\bar{\rho}(z) = (\rho_t - \rho_b)\left(\frac{z}{h} + \frac{1}{2}\right)^k + \rho_b$$

in which the material properties (E_t, G_t, and ρ_t) at the top surface ($z = h/2$) are provided by ceramic, while the bottom ones (i.e., E_b, G_b, and ρ_b) are given by metal. It is worth noting that the positive real number k ($0 \leq k \leq \infty$) is related to the material variation profile through the thickness.

Before applying the DSC method, it is necessary to carry out a convergence test for the selection of the half computational bandwidth (M) and the number of grid points (N). As reported by Zhang et al. [43], the grid size N has little influence on the vibration analysis of FG beams. The DSC algorithm with $N = 51$ has been validated for moving load problems. To further determine a suitable value of M, Table 1 presents the natural frequencies of FG beams with different boundaries and slenderness ratios calculated by altering M from 1 to 32. The FG beam is composed of alumina (Al_2O_3) and aluminum (Al). Computations are carried out by using the following material properties, $E_t = 380\text{GPa}$, $\rho_t = 3800\text{kg/m}^3$, $E_b = 70\text{GPa}$, $\rho_b = 2700\ \text{kg/m}^3$, and the Poisson's ratio (ν) of FG beams is assumed to be constant ($= 0.23$) [82]. The following non-dimensional natural frequency is used in this case [82]

$$\bar{\lambda} = \omega L^2 \sqrt{\frac{I_1}{h^2 \int_{-h/2}^{h/2} \bar{E}(z)\, dz}}, \quad I_1 = \int_{-h/2}^{h/2} \bar{\rho}(z)\, dz \tag{65}$$

In Table 1, the present results are compared with those given by Sina et al. [82] and Simsek [83]. It is observed that the convergent solutions can be obtained when $M \geq 17$. The non-dimensional natural frequencies of FG beams with simply supported and clamped ends and different slenderness ratios (i.e., $L/h = 10, 30\ and\ 100$) agree well with the published results. Therefore, the values of $M = 32$ and $N = 51$ are selected for subsequent analysis in this work.

To demonstrate the accuracy and reliability of the present study, illustrative numerical examples are provided. The first three non-dimensional frequencies of simply supported FG beams for various values of the power-law index k are given in Table 2. The DSC-based results are compared with those of Simsek [83] using the first-order shear deformation beam theory (FSDBT), and Zahedinejad [84] and Thai and Vo [85] based on the third shear deformation beam theory (TSDBT). The material constants in this case are $E_t = 380\text{GPa}$, $\rho_t = 3960\text{kg/m}^3$, $E_b = 70\text{GPa}$, $\rho_b = 2702\ \text{kg/m}^3$, and $\nu_t = \nu_c = 0.3$. The non-dimensional natural frequency parameter is defined by [83-85]

$$\bar{\lambda} = \frac{\omega L^2}{h}\sqrt{\frac{\rho_b}{E_b}} \tag{66}$$

The predicted fundamental frequencies for clamped FG beams are given in Table 3. It is clear that good agreement is achieved between the present results and available solutions. As expected, increasing the power-law index reduces the natural frequencies of FG beams. This is because an enhancement of bending rigidity resulted from a higher value of k. In Tables 2 and 3, the analysis results also indicate that the natural frequency will increase as the slenderness ratio increases.

To further evaluate the accuracy and reliability of the present study and investigate the effect of elastic foundation on the dynamic characteristics of FG beams ($L/h = 10$), the first three natural frequencies of simply supported and clamped beams resting on the Winkler–Pasternak foundation are calculated and compared with those by Zahedinejad [84], as presented in Tables 4 and 5. The two coefficients of the Winkler–Pasternak foundation are defined by [84]

$$\bar{k}_1 = \frac{K_1 L^2}{E_0 I}, \quad \bar{k}_2 = \frac{K_2 L^2}{\pi^2 E_0 I} \tag{67}$$

where the moment of inertia is given by $I = bh^3/12$.

In Tables 4 and 5, the parameter of shear layer foundation stiffness $\bar{k}_2$ is assumed to be constant ($= 1$) and the modulus of Winkler foundation $\bar{k}_1$ varies from 1 to 1000. In this case, the material properties are the same as those used in Table 2. Obviously, it is seen that by increasing the Winkler's elastic foundation parameter, the system stiffness increases, and consequently the non-dimensional natural frequency increases. Also, the comparison studies conducted in Tables 4 and 5 reveal the proposed method in good agreement with the published solutions.

5.2 Free vibration analysis of FG-GPLR beams resting on the Winkler–Pasternak elastic foundation

The previous section has confirmed the correctness and accuracy of the DSC method. This section will conduct a parametric study to analyze the influence of various factors, including the GPL dispersion patterns, porosity distributions, GPL weight fractions ($wt.\%$), porosity coefficients, boundary conditions, slenderness ratios, and foundation coefficients, on the natural frequencies of FG-GPLR porous beams.

Table 6 presents the non-dimensional fundamental frequency of clamped FG-GPLR porous beam with and without graphene reinforcements. As the porosity coefficient e_0 varies from 0 to 0.6 according to the distribution pattern 1, the fundamental natural frequencies decrease. It is also observed that a small amount of GPLs dispersed into metal foam can greatly strengthen the FG-GPLR beam. By altering the weight fraction of GPLs, Table 7 lists the fundamental frequency increment (%) of FG-GPLR porous beams with different slenderness ratios. The frequency increment becomes slightly higher as the slenderness ratio increases. Moreover, the present results are consistent with those solutions from the available literature.

Figure 5 illustrates the effect of GPL weight fractions on the fundamental frequency variation of FG-GPLR beams with different porosity distributions. A

clamped FG-GPLR porous beam with a slenderness ratio $L/h = 10$ is considered here as an example and the porosity coefficient $e_0 = 0.6$ is selected for all cases. No GPL nanofillers together with five different weight fractions (i.e., 0.2%, 0.4%, 0.6%, 0.8% and 1%) according to three types of dispersion patterns are considered. The effect of GPLs can remarkably enhance the effective stiffness of FG-GPLR porous beams, leading to the significant increment of vibration frequencies. In Figs. 5(a) – (c), the best reinforcement performance is found in the case of the porosity distribution type 1 for various GPL dispersion patterns. This is because the larger stiffness at the top and bottom of the beam can be achieved by the lower porosity of symmetric distribution pattern 1 among other porosity distributions. In contrast to another symmetric porosity scheme, i.e., the porosity distribution type 3 results in the lowest fundamental frequencies of FG-GPLR porous beams under the same scenario. The fundamental frequencies of FG-GPLR porous beams based on the non-symmetric porosity distribution (type 2) are very close to those from the uniform porosity distribution (type 4). Obviously, the pattern A shows the best capability to enhance the beam stiffness among all dispersion patterns.

To further explore the influence of the porosity coefficient e_0 on the vibration behavior of FG-GPLR porous beams, various coefficients, 0 to 0.9 with an interval of 0.1, are explicitly employed. A clamped beam reinforced by a 2% weight fraction of GPLs with various dispersion patterns is used for illustration. As shown in Figs. 6(b) and 5(c), the increase of porosity coefficients leads to the decrease of fundamental frequencies. However, the growth of e_0 does not always reduce the fundamental frequencies of FG-GPLR porous beams, as shown in Fig. 6(a). The frequencies would be magnified as e_0 is larger than 0.6. Figure 6(d) compares the fundamental frequencies of FG-GPLR porous beams under the dispersion pattern A. Based on the results, we found that the combination of the dispersion pattern A and the porosity distribution type 1 is the best choice of graphene reinforcements.

The influence of two elastic foundation parameters on the first natural frequencies of clamped FG-GPLR porous beams with various porosity distributions ($e_0 = 0.6$) is demonstrated in Fig. 7, in which all cases are reinforced by GPLs based on the dispersion pattern A. Four different cases, including no elastic foundation ((k_1, k_2) = (0.00, 0.00)), Winkler-type foundation ((k_1, k_2) = (0.01, 0.00)), and Winkler–Pasternak foundation ((k_1, k_2) = (0.00, 0.01) and (k_1, k_2) = (0.01, 0.01)), are presented. Note that the definitions of k_1 and k_2 are stated in Eq. (31). In all these cases, the frequency increases as the weight fraction of GPLs becomes larger. In addition, the foundation effect can considerably increase the structural stiffness, leading to higher natural frequencies. Besides, it is also found that the influence of the stiffness parameter k_2 is much more pronounced than k_1 on the fundamental frequency under the same scenario.

We then look into the effect of boundary conditions and slenderness ratios on the fundamental frequency variation of FG-GPLR porous beams. As illustrated in Fig. 8, the non-dimensional fundamental frequency increases as the slenderness ratio L/h increases in all cases. Careful examinations reveal that the results of fundamental frequencies in the simply supported case (with or without the Winkler foundation) is smaller than that of the clamped one.

5.3 Forced vibration analysis of FG-GPLR beams resting on the Winkler–Pasternak elastic foundation

In this section, we focus on the dynamic response of FG-GPLR porous beams resting on an elastic foundation subjected to a moving load. Effects of different parameters, including material properties, moving load velocities and porosity coefficients, on the dynamic characterization of such beams are studied. Prior to applying the DSC regularized Dirac-delta method for moving load problems, the

determination of an appropriate value for the regularized parameter α must be performed. For convenience and brevity, the material properties and geometry parameters of an FG beam are the same as those from Şimşek and Kocatürk [86]. The top surface of the FG beam is pure alumina (Al_2O_3) with material properties $\bar{E}_t = 390$ GPa and $\bar{\rho}_t = 3960$ kg/m^3, while the bottom surface of FG beams is made up of 100% Aluminum (Al) with the material parameters $\bar{E}_b = 210$ GPa and $\bar{\rho}_b = 7800$ kg/m^3. The Poisson's ratio $\bar{\nu}_t = \bar{\nu}_b$ is set as 0.3. The dimensions are length $L = 20$ m, width $b = 0.4$ m and height $h = 0.9$ m. The magnitude of the moving force is $f = 10^5$N. The maximum dynamic magnification factor (DMF) is defined by [87]

$$D_d = \max\left(\frac{w_0(L/2,t)}{w_{st}}\right) \tag{68}$$

where $w_0(L/2,t)$ denotes the mid-span displacement of the beam, and w_{st} is the static deflection that is equal to $fL^3/48EI$ and $fL^3/192EI$ for simply supported and clamped conditions, respectively. Equation (59) can be solved by the Newmark–β integration scheme with a time step of $n_t = 500$.

Table 8 summarizes the results calculated by the proposed method with different values of the regularized parameter (from 0.042 to 0.2). To determine an appropriate value of the regularized parameter, the results are compared with those from other methods, such as the finite element formulation based on the Timoshenko beam theory [87], mixed Ritz–DQ method [88] and Lagrange multipliers [86] using the Euler–Bernoulli beam theory. Clearly, good accuracy and agreement can be obtained by the DSC regularized Dirac-delta algorithm with $\alpha = 0.042$ for the problem being concerned. It is worth noting that the maximum DMF of an Euler–Bernoulli beam is slightly smaller than that of a Timoshenko beam, because the transverse shear deformation and rotary inertia are taken into account.

Figure 9 displays the relationship between the velocity of a moving load and the maximum DMF for various GPL weight fractions. By using different GPL dispersion patterns, Figs. 9(a)–(c) presents the dynamic response of three types of FG-GPLR beams for $v_p = 1-300\ \mathrm{m/s}$. The DSC-based results are almost identical to those obtained by Ref. [86]. Clearly, the moving load velocity has considerable impact on the dynamic behavior of FG-GPLR porous beams. In Fig. 9, the value of maximum DMF increases as the moving load velocity becomes faster until to a critical value and then decreases. The increment of GPL additives dispersed into the metal matrix results in the reduction of maximum DMF, because adding nanofillers can enhance the total stiffness of such beams. Besides, Fig. 9(d) compares the reinforcement performance of three dispersion patterns under the same GPL weight fraction (2.0%). The best improvement of the stiffness is observed in the dispersion pattern A, while the values of the maximum DMF in other two patterns (B and C) are close to each other. This is due to the fact that more GPL nanofillers added at the top and bottom sides can greatly improve the total stiffness.

In Table 9, the peak values of the maximum DMF and its corresponding velocities are presented. We observe that the DSC-based results tally with those from the existing results [87] for the pure steel and pure Al_2O_3 cases. The first-known results in Table 9 can serve as benchmark solutions. Based on the results, it is found that more GPL additives dispersed to the metal matrix are, the higher value of "critical velocity" is.

To further investigate the effect of porosity on the dynamic characteristics of an FG-GPLR beam, a total number of twelve combinations of various GPL dispersion patterns and porosity distributions ($e_0 = 0.2$) are given in Fig. 10. In all these cases, the moving point load with a speed of $131\ \mathrm{m/s}$ is exerted on the beam. In Figs. 10(a) – (c), a small amount of GPL nanofillers can lead to a remarkable reduction of maximum DMF for all combinations. For different porosity distributions, type 1 (stiffened at the

top and bottom sides with a symmetric porosity distribution) possesses the smallest maximum DMF but type 3 is the largest among these cases. The dynamic performance of type 2 is slightly better than that of type 4.

Figure 11 presents the maximum DMF for a simply supported FG-GPLR beam excited by the action of moving loads with different velocities ($v_p = 10\mathrm{m/s}$, $v_p = 20\mathrm{m/s}$, $v_p = 30\mathrm{m/s}$, and $v_p = 40\mathrm{m/s}$). The beam sits on the elastic foundations with two stiffness parameters (k_1, k_2) as (0.00, 0.00), (0.01, 0.00), (0.00, 0.01) and (0.01, 0.01). Note that the horizontal axis t is the dimensionless time of the moving point load that records the load from the left to the right end. The weight fraction of GPLs is 1.2% according to the dispersion pattern A, and the porosity coefficient e_0 is 0.2 for the cases given in Fig. 11. It is found that increasing the running speed of the moving load can lead to a smoother maximum DMF in time history, and the elastic foundation can significantly cut down the transverse deflection of beams excited by a moving load. Moreover, the effect of the Pasternak foundation is much more pronounced than that of the Winkler foundation.

6. Conclusions

This work presents a comprehensive study for the dynamic characterization of FG-GPLR porous beams supported by an elastic foundation under a moving load by means of the proposed DSC regularized Dirac-delta algorithm. In this calculation scheme, a two-level discretization (i.e., spatial and temporal), involving the approximation of the equilibrium equations and the representation of a moving load, is carried out by two kinds of the regularized delta type functions, respectively. The generated banded matrix enables trade-offs between computational effort and accuracy. The uniformly distributed grid points used in the DSC method can lead to a preferable representation of moving load vectors with the same order errors of approximation regardless of the location of a moving load. It is evident that this newly proposed approach paves an

effective way to address the difficulty of strong-from based methods for moving load problems.

To gain deeper insights into the material properties of FG-GPLR porous beams, four types of porosity distributions and three classes of GPL dispersion patterns are considered herein. A theoretical beam model is formulated by the Timoshenko beam theory and the principle of virtual work. Extensive results, most of them are first-known solutions in tabular and graphical forms, are provided to show the influence of various parameters on the vibration frequencies and mid-span transverse deflections of FG-GPLR porous beams. The major findings of this work are summarized as follows:

- The dispersion of GPLs into metal foams can remarkably improve the total stiffness of FG-GPLR porous beams, resulting in the increase of natural frequencies and the reduction of transverse deflections under the effect of a moving load.
- Among various GPL dispersion patterns, the pattern A is superior to other two patterns in view of the reinforcement performance. The patterns B and C show a comparable ability in the improvement of beam stiffness.
- Increasing the porosity coefficient can either induce the reduction or increment of fundamental frequencies, depending on the incorporation of porosity distributions and GPL dispersion patterns.
- The first type of porosity distribution is an ideal scheme as compared to other three distribution types.
- The fundamental frequency of FG-GPLR porous beams decreases as the slender ratio becomes larger.
- The Winkler–Pasternak foundation can significantly enhance the stiffness of FG-GPLR porous beams. The influence of the Pasternak foundation parameter (k_2) is much more pronounced than the Winkler foundation parameter (k_1) on the dynamic behavior of FG-GPLR porous beams under the action of a moving load.

Acknowledgements

The work described in this paper was supported by the Research Impact Fund (Project No. R-5020-18) from the Research Grants Council of the Hong Kong Special Administrative Region. In addition, the funding support from the Innovation and Technology Commission of the HKSAR Government to the Hong Kong Branch of National Rail Transit Electrification and Automation Engineering Technology Research Center (Grant Nos. K-BBY1 and 1-BBVQ) is gratefully acknowledged. The first author (L.H. Zhang) also acknowledged the financial support of the Research Student Attachment Program offered from The Hong Kong Polytechnic University, and appreciated the kind hospitality provided from The RMIT University during his academic visit at that institution.

Appendix A

The virtual variation expressions of the kinetic energy (δT), strain energy (δV_s), potential energy (δV_w), and work done due to an external moving load (δQ) are given by

$$\delta T = -b\int_0^l \left[\left(I_0\frac{\partial^2 u_0}{\partial t^2} - I_1\frac{\partial^2 \phi}{\partial t^2}\right)\delta u_0 + \left(-I_1\frac{\partial^2 u_0}{\partial t^2} + I_2\frac{\partial^2 \phi}{\partial t^2}\right)\delta\phi + I_0\frac{\partial^2 w_0}{\partial t^2}\delta w_0\right]dx \tag{A1}$$

$$\delta V_s = -b\int_0^l \left[\left(A_{11}\frac{\partial^2 u_0}{\partial x^2} - B_{11}\frac{\partial^2 \phi}{\partial x^2}\right)\delta u_0 + \left(-B_{11}\frac{\partial^2 u_0}{\partial x^2} + D_{11}\frac{\partial^2 \phi}{\partial x^2} + A_{55}\frac{\partial w_0}{\partial x} - A_{55}\phi\right)\delta\phi + \left(A_{55}\frac{\partial^2 w_0}{\partial x^2} - A_{55}\frac{\partial \phi}{\partial x}\right)\delta w_0\right]dx \tag{A2}$$

$$\delta V_w = b\int_0^l \left(K_1 w_0 - K_2\frac{\partial^2 w_0}{\partial x^2}\right)\delta w_0 dx \tag{A3}$$

$$\delta Q = b\int_0^l f\delta(x - v_p t)\delta w_0 dx \tag{A4}$$

Appendix B

The elements of the stiffness matrix $[\mathbf{K}]$ and mass matrix $[\mathbf{M}]$ in Eq. (59) are given by

$$[\mathbf{K_{aa}}] = (a_{55} + k_2)\left[\mathbf{D}^2_{W_\xi}\right] - k_1[\mathbf{I}] \tag{B1}$$

$$[\mathbf{K_{ab}}] = -a_{55}\eta\left[\mathbf{D}^1_{\Phi_\xi}\right] \tag{B2}$$

$$[\mathbf{K_{ba}}] = a_{55}\eta\left[\mathbf{D}^1_{W_\xi}\right] \tag{B3}$$

$$[\mathbf{K_{bb}}] = \left(d_{11} - \frac{{b_{11}}^2}{a_{11}}\right)\left[\mathbf{D}^2_{\Phi_\xi}\right] - a_{55}\eta^2[\mathbf{I}] \tag{B4}$$

$$[\mathbf{M_{aa}}] = -i_0[\mathbf{I}] \tag{B5}$$

$$[\mathbf{M_{ab}}] = [\mathbf{0}] \tag{B6}$$

$$[\mathbf{M_{ba}}] = [\mathbf{0}] \tag{B7}$$

$$[\mathbf{M_{bb}}] = \left(\frac{b_{11}i_1}{a_{11}} - i_2\right)[\mathbf{I}] \tag{B8}$$

in which $[\mathbf{I}]$ represents an $N \times N$ identity matrix.

In Eq. (59), the lateral deflection vector $\{\boldsymbol{W_0}(t)\}$, rotation vector $\{\boldsymbol{\Phi}(t)\}$, and acceleration vectors $\{\ddot{\boldsymbol{W}}_{\mathbf{0}}(t)\}$, $\{\ddot{\boldsymbol{\Phi}}(t)\}$ are presented as

$$\{\boldsymbol{W_0}(t)\} = \{W_0(\xi_0, t) \quad W_0(\xi_1, t) \quad \cdots \quad W_0(\xi_{N-1}, t)\}^T \tag{B9}$$

$$\{\ddot{\boldsymbol{W}}_{\mathbf{0}}(t)\} = \{\ddot{W}_0(\xi_0, t) \quad \ddot{W}_0(\xi_1, t) \quad \cdots \quad \ddot{W}_0(\xi_{N-1}, t)\}^T \tag{B10}$$

$$\{\boldsymbol{\Phi}(t)\} = \{\Phi(\xi_0, t) \quad \Phi(\xi_1, t) \quad \cdots \quad \Phi(\xi_{N-1}, t)\}^T \tag{B11}$$

$$\{\ddot{\boldsymbol{\Phi}}(t)\} = \{\ddot{\Phi}(\xi_0, t) \quad \ddot{\Phi}(\xi_1, t) \quad \cdots \quad \ddot{\Phi}(\xi_{N-1}, t)\}^T \tag{B12}$$

Besides, the load vector $\{\boldsymbol{F}(t)\}$ that can be approximated by the regularized Gauss' delta function via Eq. (46) is written as

$$\{\boldsymbol{F}(t)\} = -\frac{F}{\sqrt{2\pi}\varepsilon}\left\{\exp\left[-\frac{\left(\xi_0 - \xi_p(t)\right)^2}{2\varepsilon^2}\right] \quad \cdots \quad \exp\left[-\frac{\left(\xi_{N-1} - \xi_p(t)\right)^2}{2\varepsilon^2}\right]\right\}^T \tag{B13}$$

In Eq. (63), the matrix elements are expressed as

$$\left[\widetilde{\mathbf{K}}_{\boldsymbol{aa}}\right] = (a_{55} + k_2)/G_1\left[\mathbf{D}^2_{W_\xi}\right] - k_1/G_1[\mathbf{I}] \tag{B14}$$

$$\left[\widetilde{\mathbf{K}}_{\boldsymbol{ab}}\right] = -a_{55}\eta/G_1\left[\mathbf{D}^1_{\Phi_\xi}\right] \tag{B15}$$

$$\left[\widetilde{\mathbf{K}}_{\boldsymbol{ba}}\right] = a_{55}\eta/G_2\left[\mathbf{D}^1_{W_\xi}\right] \tag{B16}$$

$$\left[\widetilde{\mathbf{K}}_{\boldsymbol{bb}}\right] = \left(d_{11} - \frac{{b_{11}}^2}{a_{11}}\right)/G_2\left[\mathbf{D}^2_{\Phi_\xi}\right] - a_{55}\eta^2/G_2[\mathbf{I}] \tag{B17}$$

where $G_1 = -i_0$ and $G_2 = b_{11}i_1/a_{11} - i_2$.

References

[1] K.I. Winey, R.A. Vaia, Polymer nanocomposites, MRS bulletin, 32 (2007) 314-322.

[2] S. Iijima, Helical microtubules of graphitic carbon, nature, 354 (1991) 56-58.

[3] E.W. Wong, P.E. Sheehan, C.M. Lieber, Nanobeam mechanics: elasticity, strength, and toughness of nanorods and nanotubes, science, 277 (1997) 1971-1975.

[4] M.S. Shaffer, A.H. Windle, Fabrication and characterization of carbon nanotube/poly (vinyl alcohol) composites, Advanced materials, 11 (1999) 937-941.

[5] F.H. Gojny, M.H. Wichmann, B. Fiedler, K. Schulte, Influence of different carbon nanotubes on the mechanical properties of epoxy matrix composites–a comparative study, Composites Science and Technology, 65 (2005) 2300-2313.

[6] M.M. Ardestani, L. Zhang, K. Liew, Isogeometric analysis of the effect of CNT orientation on the static and vibration behaviors of CNT-reinforced skew composite plates, Computer Methods in Applied Mechanics and Engineering, 317 (2017) 341-379.

[7] Z. Pan, L. Zhang, K. Liew, Modeling geometrically nonlinear large deformation behaviors of matrix cracked hybrid composite deep shells containing CNTRC layers, Computer Methods in Applied Mechanics and Engineering, 355 (2019) 753-778.

[8] N.D. Duc, S.-E. Kim, T.Q. Quan, D.T. Manh, N.H. Cuong, Nonlinear buckling of eccentrically stiffened nanocomposite cylindrical panels in thermal environments, Thin-Walled Structures, 146 (2020) 106428.

[9] P.D. Nguyen, V.D. Quang, V.T.T. Anh, N.D. Duc, Nonlinear vibration of carbon nanotube reinforced composite truncated conical shells in thermal environment, International Journal of Structural Stability and Dynamics, (2019).

[10] I. Zaman, T.T. Phan, H.-C. Kuan, Q. Meng, L.T.B. La, L. Luong, O. Youssf, J. Ma, Epoxy/graphene platelets nanocomposites with two levels of interface strength, Polymer, 52 (2011) 1603-1611.

[11] M. Dresselhaus, G. Dresselhaus, R. Saito, Physics of carbon nanotubes, Carbon, 33 (1995) 883-891.

[12] S. Reich, C. Thomsen, J. Maultzsch, Carbon nanotubes: basic concepts and physical properties, John Wiley & Sons, 2008.

[13] K.M. Liew, Y. Jianwei, L.-W. Zhang, Mechanical behaviors of carbon nanotubes: theoretical and numerical approaches, William Andrew, 2016.

[14] B. Kumanek, D. Janas, Thermal conductivity of carbon nanotube networks: A review, Journal of materials science, 54 (2019) 7397-7427.

[15] Y.-Y. Zhang, Q.-X. Pei, Y.-W. Mai, S.-K. Lai, Interfacial thermal conductance in multilayer graphene/phosphorene heterostructure, Journal of Physics D: Applied Physics, 49 (2016) 465301.

[16] I. Duarte, E. Ventura, S. Olhero, J.M. Ferreira, An effective approach to reinforced closed-cell Al-alloy foams with multiwalled carbon nanotubes, Carbon, 95 (2015) 589-600.

[17] I. Duarte, E. Ventura, S. Olhero, J.M. Ferreira, A novel approach to prepare aluminium-alloy foams reinforced by carbon-nanotubes, Materials Letters, 160 (2015) 162-166.

[18] H.-S. Shen, Functionally graded materials: nonlinear analysis of plates and shells, CRC press, 2016.

[19] P. Zahedinejad, C. Zhang, H. Zhang, S. Ju, A Comprehensive Review on Vibration Analysis of Functionally Graded Beams, International Journal of Structural Stability and Dynamics, (2020) 2030002.
[20] S. Zhao, Z. Zhao, Z. Yang, L. Ke, S. Kitipornchai, J. Yang, Functionally graded graphene reinforced composite structures: A review, Engineering Structures, 210 (2020) 110339.
[21] N. Duc, Nonlinear static and dynamic stability of functionally graded plates and shells, Hanoi:, (2014).
[22] N.D. Duc, N.D. Tuan, P. Tran, N.T. Dao, N.T. Dat, Nonlinear dynamic analysis of Sigmoid functionally graded circular cylindrical shells on elastic foundations using the third order shear deformation theory in thermal environments, International Journal of Mechanical Sciences, 101 (2015) 338-348.
[23] D.D. Nguyen, Nonlinear thermo-electro-mechanical dynamic response of shear deformable piezoelectric sigmoid functionally graded sandwich circular cylindrical shells on elastic foundations, Journal of Sandwich Structures & Materials, 20 (2018) 351-378.
[24] N.D. Khoa, H.T. Thiem, N.D. Duc, Nonlinear buckling and postbuckling of imperfect piezoelectric S-FGM circular cylindrical shells with metal–ceramic–metal layers in thermal environment using Reddy's third-order shear deformation shell theory, Mechanics of Advanced Materials and Structures, 26 (2019) 248-259.
[25] P.P. Minh, N.D. Duc, The effect of cracks on the stability of the functionally graded plates with variable-thickness using HSDT and phase-field theory, Composites Part B: Engineering, 175 (2019) 107086.
[26] M. Vinyas, S.C. Kattimani, Static analysis of stepped functionally graded magneto-electro-elastic plates in thermal environment: a finite element study, Composite Structures, 178 (2017) 63-86.
[27] M. Vinyas, S.C. Kattimani, Static studies of stepped functionally graded magneto-electro-elastic beam subjected to different thermal loads, Composite Structures, 163 (2017) 216-237.
[28] K.S. Novoselov, A.K. Geim, S.V. Morozov, D. Jiang, Y. Zhang, S.V. Dubonos, I.V. Grigorieva, A.A. Firsov, Electric field effect in atomically thin carbon films, science, 306 (2004) 666-669.
[29] H.-S. Shen, Nonlinear bending of functionally graded carbon nanotube-reinforced composite plates in thermal environments, Composite Structures, 91 (2009) 9-19.
[30] M. Song, S. Kitipornchai, J. Yang, Free and forced vibrations of functionally graded polymer composite plates reinforced with graphene nanoplatelets, Composite Structures, 159 (2017) 579-588.
[31] C. Feng, S. Kitipornchai, J. Yang, Nonlinear bending of polymer nanocomposite beams reinforced with non-uniformly distributed graphene platelets (GPLs), Composites Part B: Engineering, 110 (2017) 132-140.
[32] S. Kitipornchai, D. Chen, J. Yang, Free vibration and elastic buckling of functionally graded porous beams reinforced by graphene platelets, Materials & Design, 116 (2017) 656-665.
[33] H.-S. Shen, Y. Xiang, Y. Fan, D. Hui, Nonlinear vibration of functionally graded graphene-reinforced composite laminated cylindrical panels resting on elastic foundations in thermal environments, Composites Part B: Engineering, 136 (2018) 177-186.
[34] H.-S. Shen, Y. Xiang, Postbuckling of functionally graded graphene-reinforced composite laminated cylindrical shells subjected to external pressure in thermal environments, Thin-Walled Structures, 124 (2018) 151-160.

[35] H.-S. Shen, Y. Xiang, F. Lin, Nonlinear vibration of functionally graded graphene-reinforced composite laminated plates in thermal environments, Computer Methods in Applied Mechanics and Engineering, 319 (2017) 175-193.
[36] Y.-B. Yang, J.-D. Yau, L.-C. Hsu, Vibration of simple beams due to trains moving at high speeds, Engineering structures, 19 (1997) 936-944.
[37] S. Law, X. Zhu, Dynamic behavior of damaged concrete bridge structures under moving vehicular loads, Engineering Structures, 26 (2004) 1279-1293.
[38] J. Yang, Y. Chen, Y. Xiang, X. Jia, Free and forced vibration of cracked inhomogeneous beams under an axial force and a moving load, Journal of Sound and Vibration, 312 (2008) 166-181.
[39] S.-M. Kim, Vibration and stability of axial loaded beams on elastic foundation under moving harmonic loads, Engineering Structures, 26 (2004) 95-105.
[40] P. Malekzadeh, S. Monajjemzadeh, Dynamic response of functionally graded beams in a thermal environment under a moving load, Mechanics of Advanced Materials and Structures, 23 (2016) 248-258.
[41] W.-Y. He, S. Zhu, Moving load-induced response of damaged beam and its application in damage localization, Journal of Vibration and Control, 22 (2016) 3601-3617.
[42] C. Svedholm, A. Zangeneh, C. Pacoste, S. François, R. Karoumi, Vibration of damped uniform beams with general end conditions under moving loads, Engineering Structures, 126 (2016) 40-52.
[43] L. Zhang, S. Lai, J. Yang, A DSC Regularized Dirac-Delta Method for Flexural Vibration of Elastically Supported FG Beams Subjected to a Moving Load, International Journal of Structural Stability and Dynamics, 20 (2020) 2050039.
[44] Y.-B. Yang, J. Yau, Z. Yao, Y. Wu, Vehicle-bridge interaction dynamics: with applications to high-speed railways, World Scientific, 2004.
[45] L. Auersch, The effect of critically moving loads on the vibrations of soft soils and isolated railway tracks, Journal of Sound and Vibration, 310 (2008) 587-607.
[46] N.D. Beskou, D.D. Theodorakopoulos, Dynamic effects of moving loads on road pavements: a review, Soil Dynamics and Earthquake Engineering, 31 (2011) 547-567.
[47] H. Xia, H. Li, W. Guo, G. De Roeck, Vibration resonance and cancellation of simply supported bridges under moving train loads, Journal of Engineering Mechanics, 140 (2014) 04014015.
[48] Y. Wang, L. Tham, Y. Cheung, Beams and plates on elastic foundations: a review, Progress in Structural Engineering and Materials, 7 (2005) 174-182.
[49] B. Ghosh, B. Fatahi, H. Khabbaz, J.-H. Yin, Analytical study for double-layer geosynthetic reinforced load transfer platform on column improved soft soil, Geotextiles and Geomembranes, 45 (2017) 508-536.
[50] K.-M. Liew, Y. Xiang, S. Kitipornchai, C. Wang, Vibration of Mindlin plates: programming the p-version Ritz method, Elsevier, 1998.
[51] F.F. Çalım, Dynamic analysis of beams on viscoelastic foundation, European Journal of Mechanics-A/Solids, 28 (2009) 469-476.
[52] T. Yan, S. Kitipornchai, J. Yang, X.Q. He, Dynamic behaviour of edge-cracked shear deformable functionally graded beams on an elastic foundation under a moving load, Composite Structures, 93 (2011) 2992-3001.

[53] M. Şimşek, T. Kocatürk, Ş. Akbaş, Dynamic behavior of an axially functionally graded beam under action of a moving harmonic load, Composite Structures, 94 (2012) 2358-2364.
[54] J.K. Lee, S. Jeong, J. Lee, Natural frequencies for flexural and torsional vibrations of beams on Pasternak foundation, Soils and Foundations, 54 (2014) 1202-1211.
[55] H. Deng, W. Cheng, S. Zhao, Vibration and buckling analysis of double-functionally graded Timoshenko beam system on Winkler-Pasternak elastic foundation, Composite Structures, 160 (2017) 152-168.
[56] S. Qaderi, F. Ebrahimi, M. Vinyas, Dynamic analysis of multi-layered composite beams reinforced with graphene platelets resting on two-parameter viscoelastic foundation, The European Physical Journal Plus, 134 (2019) 339.
[57] D. Froio, E. Rizzi, F.M. Simões, A.P. Da Costa, Universal analytical solution of the steady-state response of an infinite beam on a Pasternak elastic foundation under moving load, International Journal of Solids and Structures, 132 (2018) 245-263.
[58] S. Eftekhari, A differential quadrature procedure with regularization of the Dirac-delta function for numerical solution of moving load problem, Latin American Journal of Solids and Structures, 12 (2015) 1241-1265.
[59] C.I. Gheorghiu, Spectral methods for differential problems, Casa Cărţii de Ştiinţă Cluj-Napoca, 2007.
[60] G. Wei, Y. Zhao, Y. Xiang, Discrete singular convolution and its application to the analysis of plates with internal supports. Part 1: Theory and algorithm, International Journal for Numerical Methods in Engineering, 55 (2002) 913-946.
[61] S. Lai, L. Zhang, Thermal effect on vibration and buckling analysis of thin isotropic/orthotropic rectangular plates with crack defects, Engineering Structures, 177 (2018) 444-458.
[62] X. Wang, Z. Yuan, J. Deng, A Review on the Discrete Singular Convolution Algorithm and Its Applications in Structural Mechanics and Engineering, Archives of Computational Methods in Engineering, (2019) 1-28.
[63] K. Gao, R. Li, J. Yang, Dynamic characteristics of functionally graded porous beams with interval material properties, Engineering Structures, 197 (2019) 109441.
[64] C. Wang, J.N. Reddy, K. Lee, Shear deformable beams and plates: Relationships with classical solutions, Elsevier, 2000.
[65] J.H. Affdl, J. Kardos, The Halpin-Tsai equations: a review, Polymer Engineering & Science, 16 (1976) 344-352.
[66] N.M. Newmark, A method of computation for structural dynamics, Journal of the engineering mechanics division, 85 (1959) 67-94.
[67] J. Yang, D. Chen, S. Kitipornchai, Buckling and free vibration analyses of functionally graded graphene reinforced porous nanocomposite plates based on Chebyshev-Ritz method, Composite Structures, 193 (2018) 281-294.
[68] K. Gao, W. Gao, D. Chen, J. Yang, Nonlinear free vibration of functionally graded graphene platelets reinforced porous nanocomposite plates resting on elastic foundation, Composite Structures, 204 (2018) 831-846.
[69] A.P. Roberts, E.J. Garboczi, Elastic moduli of model random three-dimensional closed-cell cellular solids, Acta materialia, 49 (2001) 189-197.

[70] A. Roberts, E.J. Garboczi, Computation of the linear elastic properties of random porous materials with a wide variety of microstructure, Proceedings of the Royal Society of London. Series A: Mathematical, Physical and Engineering Sciences, 458 (2002) 1033-1054.
[71] M.A. Rafiee, J. Rafiee, Z. Wang, H. Song, Z.-Z. Yu, N. Koratkar, Enhanced mechanical properties of nanocomposites at low graphene content, ACS nano, 3 (2009) 3884-3890.
[72] M. Shokrieh, M. Esmkhani, Z. Shokrieh, Z. Zhao, Stiffness prediction of graphene nanoplatelet/epoxy nanocomposites by a combined molecular dynamics–micromechanics method, Computational materials science, 92 (2014) 444-450.
[73] R.G. De Villoria, A. Miravete, Mechanical model to evaluate the effect of the dispersion in nanocomposites, Acta Materialia, 55 (2007) 3025-3031.
[74] D. Chen, J. Yang, S. Kitipornchai, Nonlinear vibration and postbuckling of functionally graded graphene reinforced porous nanocomposite beams, Composites Science and Technology, 142 (2017) 235-245.
[75] S.P. Timoshenko, J.M. Gere, Theory of elastic stability, Courier Corporation, 2009.
[76] X. Wang, C. Jin, Differential quadrature analysis of moving load problems, Advances in Applied Mathematics and Mechanics, 8 (2016) 536-555.
[77] G. Wei, Y. Zhao, Y. Xiang, The determination of natural frequencies of rectangular plates with mixed boundary conditions by discrete singular convolution, International Journal of Mechanical Sciences, 43 (2001) 1731-1746.
[78] C.H.W. Ng, Y.B. Zhao, G.W. Wei, Comparison of discrete singular convolution and generalized differential quadrature for the vibration analysis of rectangular plates, Computer Methods in Applied Mechanics and Engineering, 193 (2004) 2483-2506.
[79] Y. Xiang, Y. Zhao, G. Wei, Discrete singular convolution and its application to the analysis of plates with internal supports. Part 2: Applications, International Journal for Numerical Methods in Engineering, 55 (2002) 947-971.
[80] Y. Zhao, G. Wei, DSC analysis of rectangular plates with non-uniform boundary conditions, Journal of Sound Vibration, 255 (2002) 203-228.
[81] N.M. Newmark, A method of computation for structural dynamics, in, American Society of Civil Engineers, 1959.
[82] S.A. Sina, H.M. Navazi, H. Haddadpour, An analytical method for free vibration analysis of functionally graded beams, Materials & Design, 30 (2009) 741-747.
[83] M. Simsek, Fundamental frequency analysis of functionally graded beams by using different higher-order beam theories, Nuclear Engineering Design, 240 (2010) 697-705.
[84] P. Zahedinejad, Free Vibration Analysis of Functionally Graded Beams Resting on Elastic Foundation in Thermal Environment, International Journal of Structural Stability and Dynamics, 16 (2016).
[85] H.-T. Thai, T.P. Vo, Bending and free vibration of functionally graded beams using various higher-order shear deformation beam theories, International Journal of Mechanical Sciences, 62 (2012) 57-66.
[86] M. Şimşek, T. Kocatürk, Free and forced vibration of a functionally graded beam subjected to a concentrated moving harmonic load, Composite Structures, 90 (2009) 465-473.

[87] D.K. Nguyen, Q.H. Nguyen, T.T. Tran, V.T. Bui, Vibration of bi-dimensional functionally graded Timoshenko beams excited by a moving load, Acta Mechanica, 228 (2016) 141-155.
[88] S.M.R. Khalili, A.A. Jafari, S.A. Eftekhari, A mixed Ritz-DQ method for forced vibration of functionally graded beams carrying moving loads, Composite Structures, 92 (2010) 2497-2511.

Captions of Figures

Fig. 1. An FG-GPLR porous beam resting on the Winkler–Pasternak elastic foundation subjected to a moving load.

Fig. 2. Various porosity distributions of the FG-GPLR beam: (a) Type 1 (symmetric); (b) Type 2 (asymmetric); (c) Type 3 (symmetric); and (d) Type 4 (uniform).

Fig. 3. Various GPL dispersion patterns on the cross-section of an FG-GPLR beam: (a) Pattern A (symmetric); (b) Pattern B (asymmetric); and (c) Pattern C (uniform).

Fig. 4. Sketch of grid point distribution between inner and fictitious/ghost points.

Fig. 5. Effect of GPL weight fraction ($wt.\%$) with different dispersion patterns on the fundamental frequency: (a) Pattern A; (b) Pattern B; (c) Pattern C; and (d) comparison results of these three patterns.

Fig. 6. Effect of porosity coefficient (e_0) with different porosity distributions on the fundamental frequency: (a) Distribution 1, (b) Distribution 2, (c) Distribution 3 and (d) comparison results of these three distributions.

Fig. 7. Effect of GPL weight fraction ($wt.\%$) dispersed by pattern A on the fundamental frequency for different elastic foundation coefficient with various porosity distributions: (a) Distribution 1; (b) Distribution 2; (c) Distribution 3; and (d) Distribution 4.

Fig. 8. Effect of slenderness ratio on the fundamental frequency: (a) C-C beam and (b) S-S beam.

Fig. 9. Variation of maximum DMF of simply supported FG-GPLR beams with a point load moving at different velocities: (a) Pattern A; (b) Pattern B; (c) Pattern C; and (d) comparison results of these three patterns.

Fig. 10. Effect of GPL weight fraction ($wt.\%$) with different porosity distributions on the maximum DMF: (a) Pattern A; (b) Pattern B; (c) Pattern C; and (d) comparison results of these three patterns.

Fig. 11. Maximum DMF of simply supported FG-GPLR beams with different foundation parameters under a moving load: (a) $v_p = 10\mathrm{m/s}$; (b) $v_p = 20\mathrm{m/s}$; (c) $v_p = 30\mathrm{m/s}$; and (d) $v_p = 40\mathrm{m/s}$.

Captions of Tables

Table 1. Convergence study of non-dimensional fundamental frequencies parameters $\bar{\lambda}$ of FG beam ($k = 0.3$) with different boundary conditions and slenderness ratios.

Table 2. Comparison of first three non-dimensional frequency parameter $\bar{\lambda}$ of simply supported FG beam for various material power law indexes k.

Table 3. Comparison of fundamental non-dimensional frequency parameter $\bar{\lambda}$ of clamped FG beam for various material power law indexes k.

Table 4. Comparison of first three non-dimensional frequency parameter $\bar{\lambda}$ of simply supported FG beam for various values of $\bar{k}_1$ and material power law indexes ($L/h = 10$).

Table 5. Comparison of first three non-dimensional frequency parameter $\bar{\lambda}$ of clamped FG beam for various values of k_w and material power law indexes ($L/h = 10$).

Table 6. Non-dimensional fundamental frequency parameter λ of FG-GPLR porous beams (porosity distribution type 1, GPL pattern A, clamped copper-matrix beam, $L/h = 20$).

Table 7. Influence of GPLs on the fundamental frequency parameter λ and its increment (%) of FG-GPLR beams with different slenderness ratios (porosity distribution type 1, GPL pattern A, clamped copper-matrix beam, $e_0 = 0.5$).

Table 8. Comparison of maximum DMF of the FG beam for various values of power-law index and velocity of load.

Table 9. Maximum DMF of simply supported FG-GPLR beam for various weight fractions and velocities (GPL pattern A, S-S steel-matrix beam).

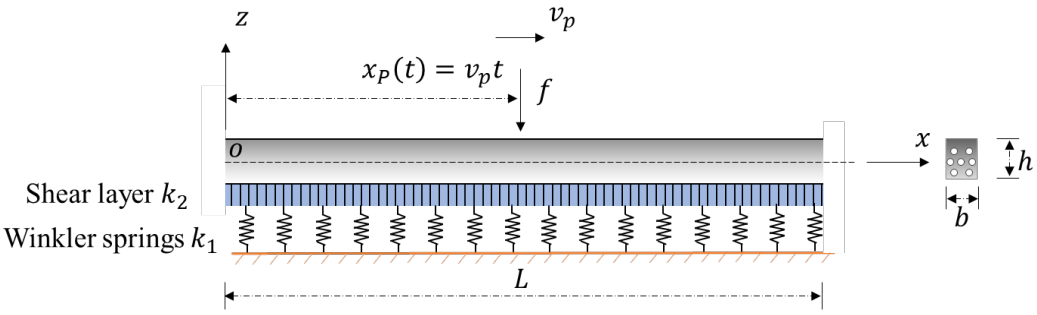

Fig. 1. An FG-GPLR porous beam resting on the Winkler–Pasternak elastic foundation subjected to a moving load.

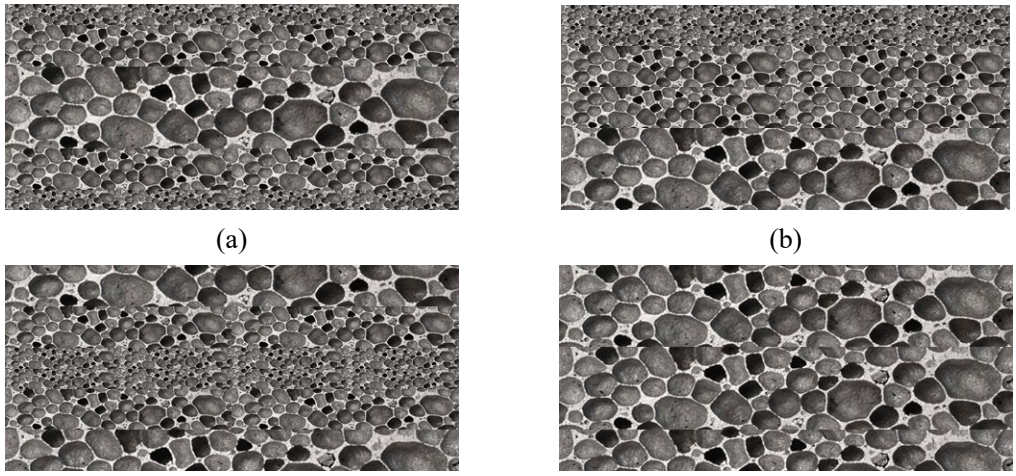

Fig. 2. Various porosity distributions of the FG-GPLR beam: (a) Type 1 (symmetric); (b) Type 2 (asymmetric); (c) Type 3 (symmetric); and (d) Type 4 (uniform).

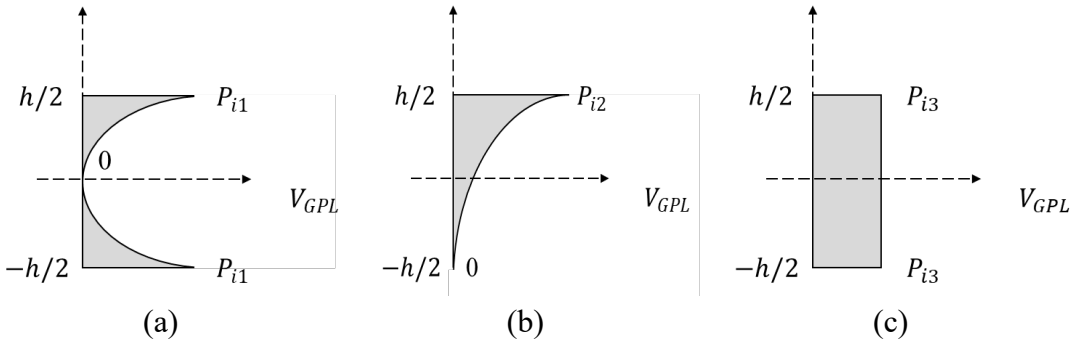

Fig. 3. Various GPL dispersion patterns on the cross-section of an FG-GPLR beam: (a) Pattern A (symmetric); (b) Pattern B (asymmetric); and (c) Pattern C (uniform).

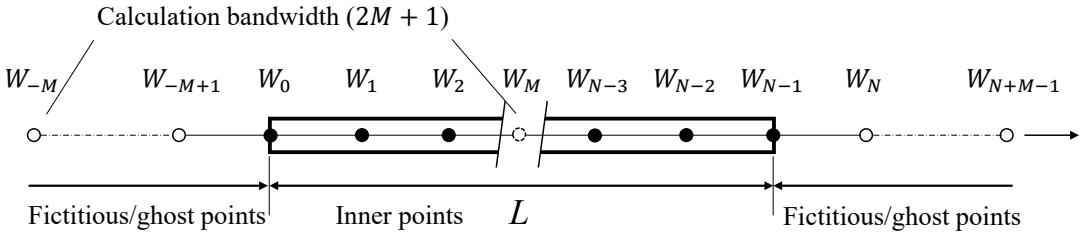

Fig. 4. Sketch of grid point distribution between inner and fictitious/ghost points.

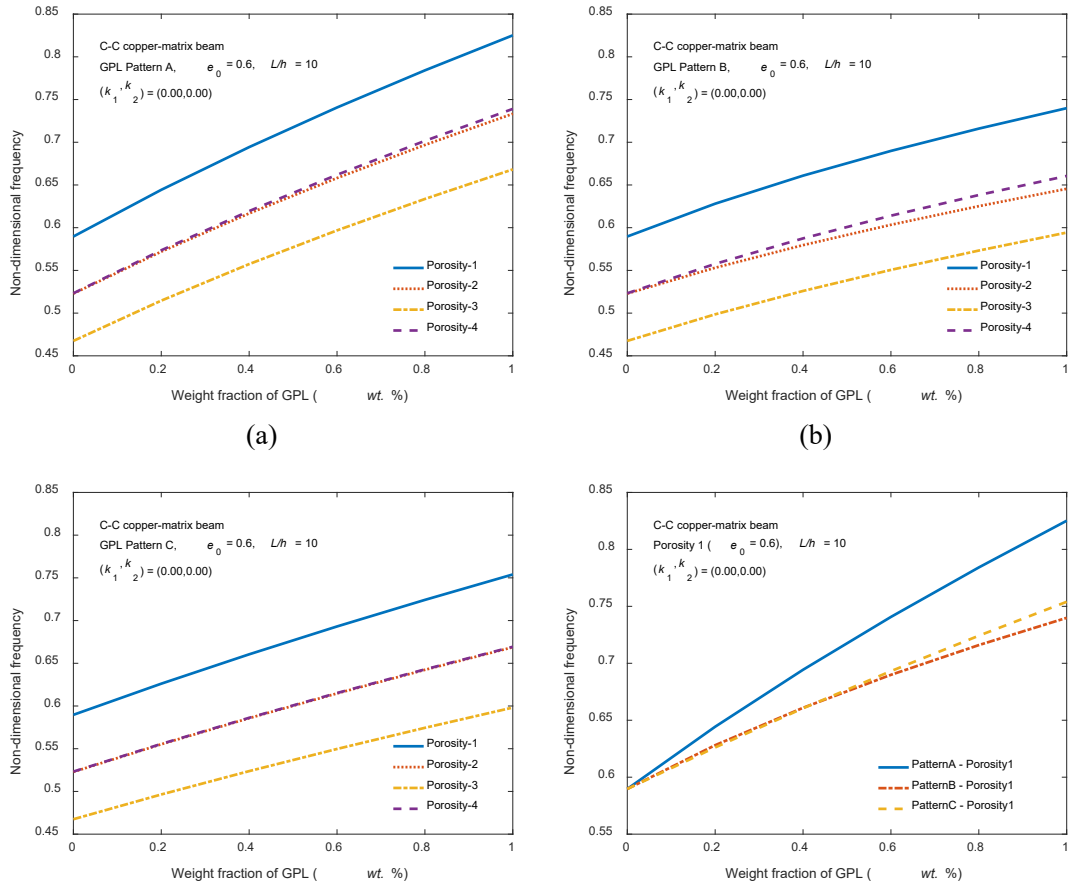

Fig. 5. Effect of GPL weight fraction ($wt.\%$) with different dispersion patterns on the fundamental frequency: (a) Pattern A; (b) Pattern B; (c) Pattern C; and (d) comparison results of these three patterns.

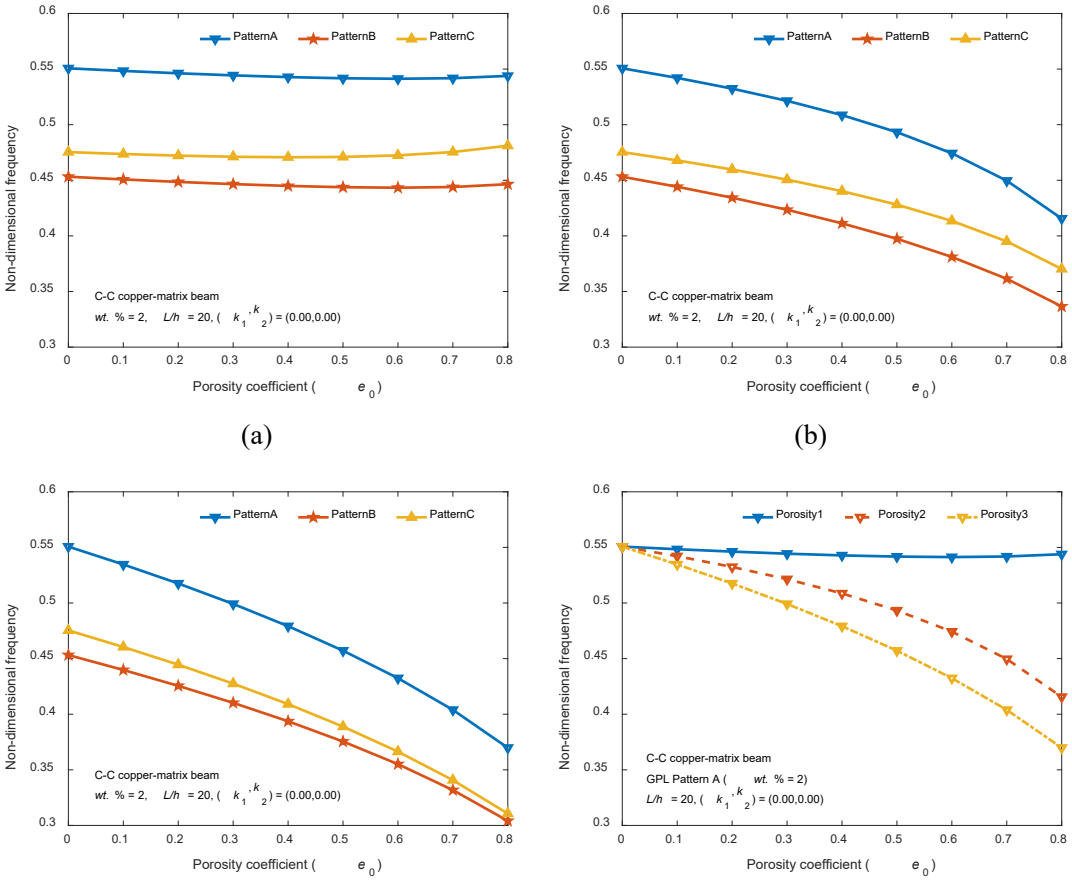

Fig. 6. Effect of porosity coefficient (e_0) with different porosity distributions on the fundamental frequency: (a) Distribution 1, (b) Distribution 2, (c) Distribution 3 and (d) comparison results of these three distributions.

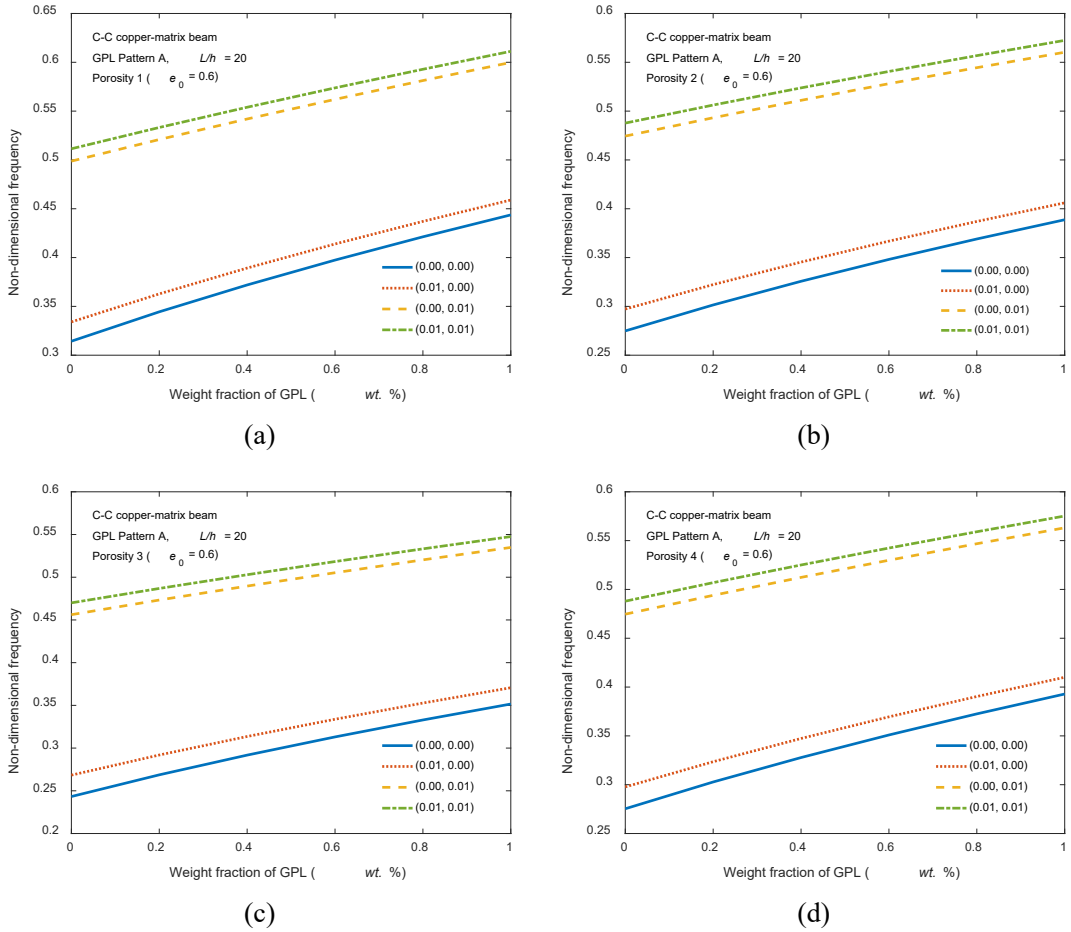

Fig. 7. Effect of GPL weight fraction ($wt.\%$) dispersed by pattern A on the fundamental frequency for different elastic foundation coefficient with various porosity distributions: (a) Distribution 1; (b) Distribution 2; (c) Distribution 3; and (d) Distribution 4.

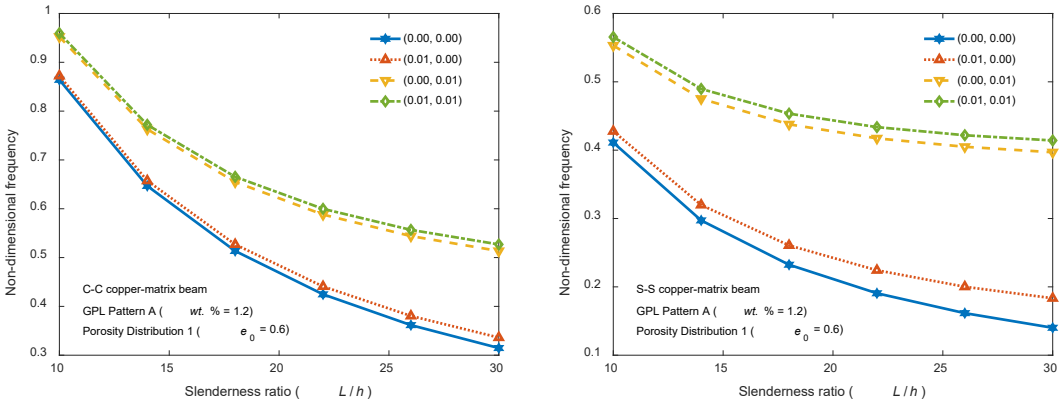

(a) (b)

Fig. 8. Effect of slenderness ratio on the fundamental frequency: (a) C-C beam and (b) S-S beam.

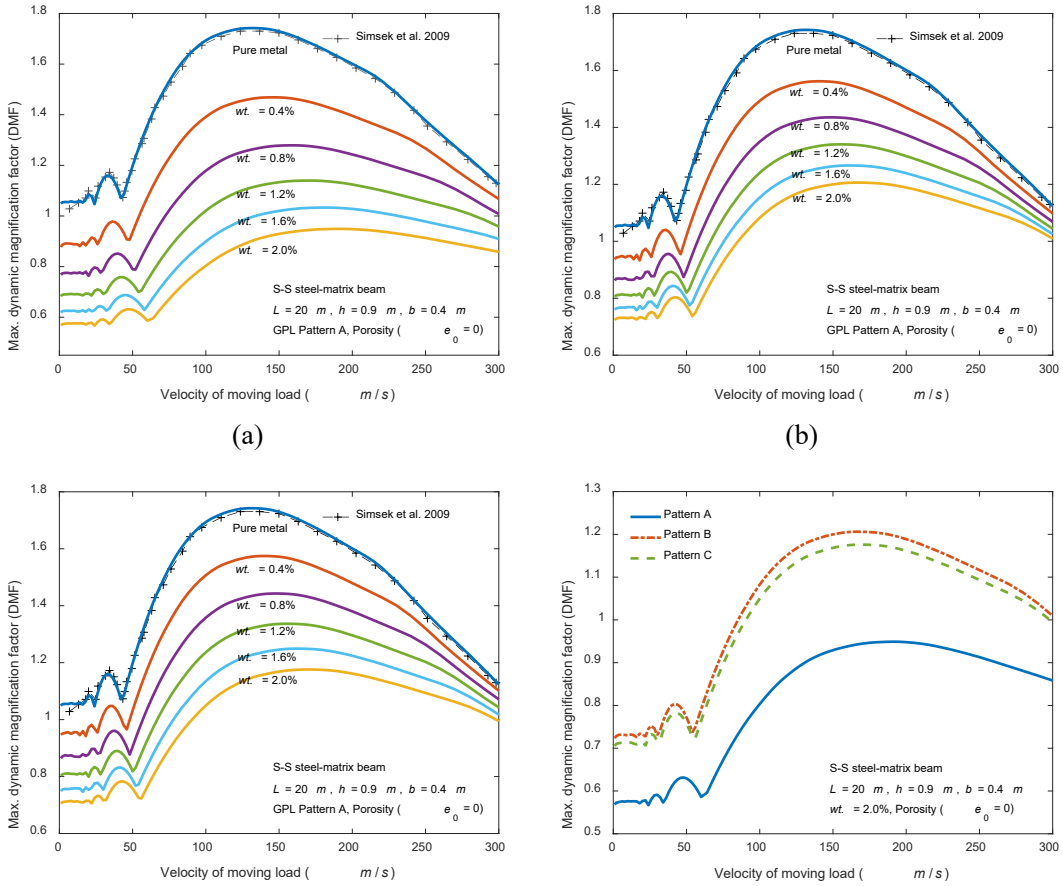

Fig. 9. Variation of maximum DMF of simply supported FG-GPLR beams with a point load moving at different velocities: (a) Pattern A; (b) Pattern B; (c) Pattern C; and (d) comparison results of these three patterns.

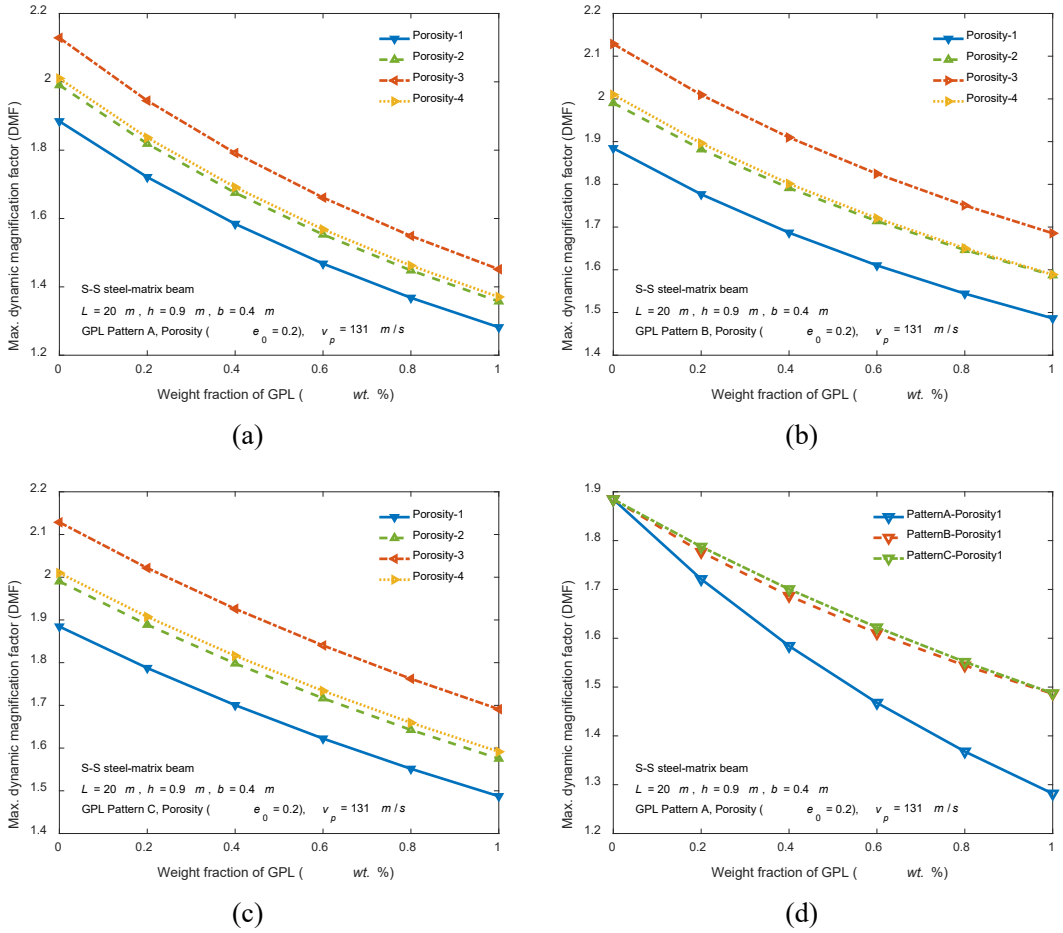

Fig. 10. Effect of GPL weight fraction ($wt.\%$) with different porosity distributions on the maximum DMF: (a) Pattern A; (b) Pattern B; (c) Pattern C; and (d) comparison results of these three patterns.

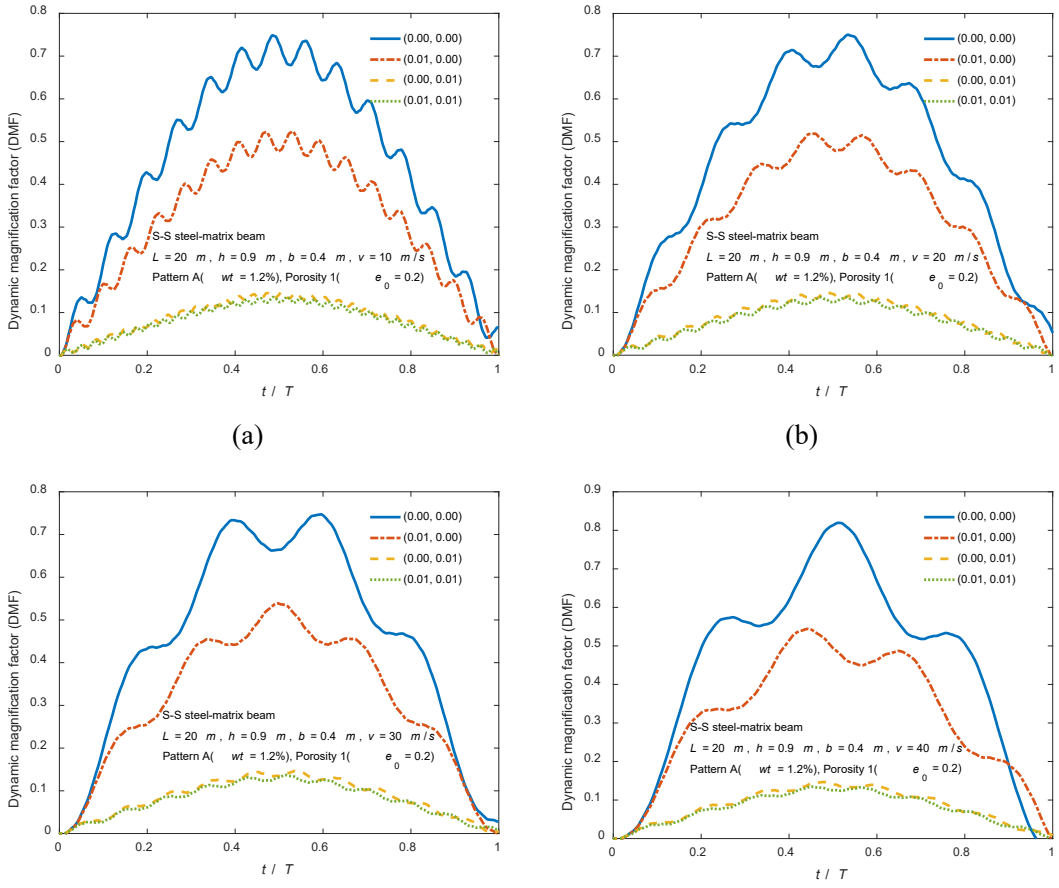

Fig. 11. Maximum DMF of simply supported FG-GPLR beams with different foundation parameters under a moving load: (a) $v_p = 10\text{m/s}$; (b) $v_p = 20\text{m/s}$; (c) $v_p = 30\text{m/s}$; and (d) $v_p = 40\text{m/s}$.

Table 1. Convergence study of non-dimensional fundamental frequencies parameters $\bar{\lambda}$ of FG beam ($k = 0.3$) with different boundary conditions and slenderness ratios.

M	$S-S$			$C-C$		
$(N = 51)$	$L/h = 10$	$L/h = 30$	$L/h = 100$	$L/h = 10$	$L/h = 30$	$L/h = 100$
5	51.176	124.309	142.734	52.224	125.78	168.437
7	11.797	54.033	108.070	19.953	57.104	172.283
10	8.038	17.953	48.8150	9.442	21.404	50.610
13	2.454	10.954	11.583	5.751	5.199	16.954
15	2.689	2.640	1.299	5.852	6.131	5.716
17	2.700	2.735	2.710	5.857	6.173	6.198
20	2.700	2.738	2.742	5.857	6.174	6.214
23	2.700	2.738	2.742	5.857	6.174	6.214
25	2.700	2.738	2.742	5.857	6.174	6.214
27	2.700	2.738	2.742	5.857	6.174	6.214
30	2.700	2.738	2.742	5.857	6.174	6.214
32	2.700	2.738	2.742	5.857	6.174	6.214
Ref. [82]	2.695	2.737	2.742	5.811	6.167	6.212
Ref. [83]	2.702	2.738	2.742	5.875	6.177	6.214

Table 2. Comparison of first three non-dimensional frequency parameter $\bar{\lambda}$ of simply supported FG beam for various material power law indexes k.

L/h	Mode		Power-law index (k)					
			0	0.5	1.0	2.0	5.0	10
5	$\bar{\lambda}_1$	Present	5.1525	4.4107	3.9966	3.6448	3.4418	3.3199
		Ref. [83][a]	5.1524	4.4083	3.9902	3.6344	3.4312	3.3134
		Ref. [85][b]	5.1527	4.4107	3.9904	3.6264	3.4012	3.2816
	$\bar{\lambda}_2$	Present	17.871	15.452	14.064	12.810	11.910	11.362
		Ref. [84][b]	17.879	15.457	14.009	12.640	11.542	11.023
		Ref. [85][b]	17.887	15.463	14.014	12.641	11.532	11.022
	$\bar{\lambda}_3$	Present	34.145	29.786	27.220	24.769	22.708	21.457
		Ref. [84][b]	34.206	29.836	27.096	24.315	21.715	20.555
		Ref. [85][b]	34.208	29.838	27.098	24.315	21.716	20.558
20	$\bar{\lambda}_1$	Present	5.4603	4.6511	4.2055	3.8376	3.6517	3.5421
		Ref. [83][a]	5.4603	4.6514	4.2051	3.8368	3.6509	3.5416
		Ref. [85][b]	5.4603	4.6511	4.2051	3.8361	3.6485	3.5390
	$\bar{\lambda}_2$	Present	21.573	18.396	16.642	15.184	14.424	13.973
		Ref. [84][b]	21.573	18.396	16.634	15.161	14.374	13.925
		Ref. [85][b]	21.573	18.396	16.634	15.162	14.375	13.926
	$\bar{\lambda}_3$	Present	47.592	40.653	36.803	33.572	31.807	30.754
		Ref. [84][b]	47.591	40.652	36.767	33.468	31.557	30.535
		Ref. [85][b]	47.593	40.653	36.768	33.469	31.578	30.537

[a] Based on the FSDBT.

[b] Based on the TSDBT.

Table 3. Comparison of fundamental non-dimensional frequency parameter $\bar{\lambda}$ of clamped FG beam for various material power law indexes k.

L/h		Power-law index (k)						
		0	0.2	0.5	1.0	2.0	5.0	10
5	Present	10.023	9.4059	8.6943	7.9263	7.2189	6.6733	6.3399
	Ref. [83][a]	10.034	9.4176	8.7005	7.9253	7.2113	6.6676	6.3406
	Ref. [84][b]	10.068	9.4620	8.7440	7.9480	7.1750	6.492	6.1640
20	Present	12.223	11.382	10.426	9.4324	8.6059	8.1717	7.9137
	Ref. [83][a]	12.224	11.385	10.426	9.4314	8.6040	8.1700	7.9128
	Ref. [84][b]	12.223	11.384	10.427	9.4310	8.5970	8.1430	7.8850

[a] Based on the FSDBT.

[b] Based on the TSDBT.

Table 4. Comparison of first three non-dimensional frequency parameter $\bar{\lambda}$ of simply supported FG beam for various values of $\bar{k}_1$ and material power law indexes ($L/h = 10$).

$\bar{k}_1$	$\bar{k}_2$	Mode	Source	Power-law index (k)				
				0	1	2	5	10
1	1	$\bar{\lambda}_1$	Present	5.886	4.890	4.632	4.534	4.473
			Ref. [84]	5.885	5.137	4.977	4.802	4.615
		$\bar{\lambda}_2$	Present	21.128	16.772	15.492	14.797	14.379
			Ref. [84]	21.128	16.662	15.290	14.517	14.159
		$\bar{\lambda}_3$	Present	43.965	34.743	31.876	30.067	28.972
			Ref. [84]	43.971	34.790	31.797	29.594	28.472
10	1	$\bar{\lambda}_1$	Present	5.9285	4.9513	4.7009	4.6092	4.5522
			Ref. [84]	5.9280	5.1950	5.0410	4.8740	4.6920
		$\bar{\lambda}_2$	Present	21.140	16.789	15.512	14.820	14.403
			Ref. [84]	21.140	16.679	15.310	14.540	14.183
		$\bar{\lambda}_3$	Present	43.971	34.751	31.886	30.078	28.983
			Ref. [84]	43.976	34.798	31.807	29.605	28.484
100	1	$\bar{\lambda}_1$	Present	6.342	5.528	5.343	5.308	5.278
			Ref. [84]	6.342	5.747	5.644	5.537	5.399
		$\bar{\lambda}_2$	Present	21.257	16.965	15.714	15.047	14.645
			Ref. [84]	21.257	16.853	15.510	14.765	14.424
		$\bar{\lambda}_3$	Present	44.026	34.835	31.983	30.188	29.102
			Ref. [84]	44.032	34.880	31.902	29.715	28.603
1000	1	$\bar{\lambda}_1$	Present	9.534	9.536	9.642	9.859	9.9624
			Ref. [84]	9.539	9.664	9.811	9.985	10.027
		$\bar{\lambda}_2$	Present	22.398	18.629	17.611	17.151	16.868
			Ref. [84]	22.398	18.504	17.382	16.851	16.641
		$\bar{\lambda}_3$	Present	44.576	35.656	32.934	31.266	30.258
			Ref. [84]	44.582	35.691	32.837	30.792	29.768

Table 5. Comparison of first three non-dimensional frequency parameter $\bar{\lambda}$ of clamped FG beam for various values of $\bar{k}_1$ and material power law indexes ($L/h = 10$).

$\bar{k}_1$	$\bar{k}_2$	Mode	Source	Power-law index (k)				
				0	1	2	5	10
1	1	$\bar{\lambda}_1$	Present	11.943	9.486	8.758	8.346	8.096
			Ref. [84]	11.949	9.486	8.731	8.260	8.009
		$\bar{\lambda}_2$	Present	30.323	24.045	22.067	20.757	19.959
			Ref. [84]	30.815	24.340	22.214	20.681	19.913
		$\bar{\lambda}_3$	Present	54.628	43.458	39.760	37.013	35.342
			Ref. [84]	54.751	43.423	39.365	35.950	34.345
10	1	$\bar{\lambda}_1$	Present	11.964	9.518	8.794	8.387	8.140
			Ref. [84]	11.969	9.517	8.768	8.302	8.054
		$\bar{\lambda}_2$	Present	30.331	24.057	22.081	20.774	19.977
			Ref. [84]	30.823	24.352	22.229	20.698	19.930
		$\bar{\lambda}_3$	Present	54.633	43.464	39.767	37.022	35.352
			Ref. [84]	54.756	43.430	39.373	35.958	34.355
100	1	$\bar{\lambda}_1$	Present	12.175	9.830	9.153	8.789	8.567
			Ref. [84]	12.180	9.829	9.127	8.707	8.485
		$\bar{\lambda}_2$	Present	30.413	24.180	22.224	20.936	20.152
			Ref. [84]	30.903	24.474	22.370	20.860	20.106
		$\bar{\lambda}_3$	Present	54.678	43.531	39.845	37.112	35.450
			Ref. [84]	54.800	43.497	39.451	36.050	34.456
1000	1	$\bar{\lambda}_1$	Present	14.106	12.529	12.173	12.095	12.033
			Ref. [84]	14.111	12.526	12.150	12.032	11.973
		$\bar{\lambda}_2$	Present	31.223	25.377	23.605	22.499	21.825
			Ref. [84]	31.701	25.653	23.735	22.423	21.780
		$\bar{\lambda}_3$	Present	55.125	44.195	40.617	38.001	36.412
			Ref. [84]	55.246	44.157	40.223	36.959	35.442

Table 6. Non-dimensional fundamental frequency parameter λ of FG-GPLR porous beams (porosity distribution type 1, GPL pattern A, clamped copper-matrix beam, $L/h = 20$).

Γ_{GPL}	Source	$e_0 = 0$	$e_0 = 0.2$	$e_0 = 0.4$	$e_0 = 0.6$
1 $wt.\%$	Present	0.4506	0.4470	0.4444	0.4437
	Ref. [32]	0.4505	0.4468	0.4442	0.4436
0 $wt.\%$	Present	0.3167	0.3145	0.3133	0.3143
(pure metal form)	Ref. [32]	0.3167	0.3144	0.3132	0.3142

Table 7. Influence of GPLs on the fundamental frequency parameter λ and its increment (%) of FG-GPLR beams with different slenderness ratios (porosity distribution type 1, GPL pattern A, clamped copper-matrix beam, $e_0 = 0.5$).

Γ_{GPL} (wt.%)	Source	$L/h = 20$		$L/h = 30$		$L/h = 40$		$L/h = 50$	
		Freq.	Incr.	Freq.	Incr.	Freq.	Incr.	Freq.	Incr.
0.0	Present	0.3135	0.00	0.2116	0.00	0.1594	0.00	0.1278	0.00
	Ref. [32]	-	0.00	-	0.00	-	0.00	-	0.00
0.2	Present	0.3438	9.68	0.2322	9.75	0.1750	9.78	0.1403	9.79
	Ref. [32]	-	9.58	-	9.65	-	9.68	-	9.69
0.4	Present	0.3715	18.52	0.2510	18.66	0.1892	18.70	0.1517	18.73
	Ref. [32]	-	18.34	-	18.47	-	18.52	-	18.54
0.6	Present	0.3972	26.71	0.2685	26.89	0.2023	26.96	0.1622	26.99
	Ref. [32]	-	26.45	-	26.63	-	26.70	-	26.73
0.8	Present	0.4212	34.35	0.2848	34.59	0.2146	34.68	0.1721	34.72
	Ref. [32]	-	34.03	-	34.26	-	34.35	-	34.39
1.0	Present	0.4437	41.55	0.3001	41.84	0.2262	41.94	0.1814	41.99
	Ref. [32]	-	41.17	-	41.45	-	41.55	-	41.60

Table 8. Comparison of maximum DMF of the FG beam for various values of power-law index and velocity of load.

Parameter in	Power-law index and moving speed of the load (m/s)					
Dirac-delta	$k = 0$	$k = 0.2$	$k = 0.5$	$k = 1.0$	$k = 2.0$	$k = \infty$
function (ε)	$v_p = 252$	$v_p = 222$	$v_p = 198$	$v_p = 179$	$v_p = 164$	$v_p = 132$
0.200	0.7753	0.8597	0.9510	1.0391	1.1117	1.4401
0.160	0.8272	0.9173	1.0146	1.1085	1.1861	1.5364
0.120	0.8744	0.9696	1.0724	1.1717	1.2538	1.6240
0.080	0.9128	1.0122	1.1196	1.2232	1.3088	1.6952
0.060	0.9277	1.0288	1.1378	1.2431	1.3302	1.7229
0.050	0.9339	1.0357	1.1454	1.2514	1.3391	1.7344
0.046	0.9361	1.0381	1.1482	1.2544	1.3423	1.7385
0.044	0.9372	1.0393	1.1495	1.2558	1.3438	1.7405
0.042	0.9382	1.0404	1.1507	1.2571	1.3453	1.7424
Ref. [87][a]	0.9380	1.0402	1.1505	1.2566	1.3446	1.7420
Ref. [88][b]	0.9317	1.0333	1.1429	1.2486	1.3360	1.7302
Ref. [86][b]	0.9328	1.0344	1.1444	1.2503	1.3376	1.7324

[a] Based on the Timoshenko beam theory.

[b] Based on the Euler–Bernoulli beam theory.

Table 9. Maximum DMF of simply supported FG-GPLR beam for various weight fractions and velocities (GPL pattern A, S-S steel-matrix beam).

		GPL weight fraction (%)						
	Source	Pure Steel	Pure Al_2O_3	0.4	0.8	1.2	1.6	2.0
Max(D_d)	Present	1.7424	0.9382	1.4687	1.2791	1.1399	1.0333	0.9490
	Ref. [87]	1.7420	0.9380	-	-	-	-	-
v_p(m/s)	Present	131	251	147	160	171	182	192
	Ref. [87]	130	251	-	-	-	-	-